On the mechanical modeling of the extreme softening/stiffening response of axially loaded tensegrity prisms

F. Fraternali, G. Carpentieri, A. Amendola

Department of Civil Engineering, University of Salerno,84084 Fisciano(SA), Italy

Abstract

We study the geometrically nonlinear behavior of uniformly compressed tensegrity prisms through fully elastic and rigid–elastic models. The given models predict a variety of mechanical behaviors in the regime of large displacements, including an extreme stiffening-type response, already known in the literature, and a newly discovered, extreme softening behavior. The latter may lead to a snap buckling event producing an axial collapse of the structure. The switching from one mechanical regime to another depends on the aspect ratio of the structure, the magnitude of the applied prestress, and the material properties of the constituent elements. We discuss potential mechanical and acoustic applications of such behaviors, which are related to the design and manufacture of tensegrity lattices and innovative metamaterials.

Keywords: Tensegrity prisms, Geometric nonlinearities, Elastic stiffening, Elastic Softening, Periodic lattices, Nonlinear metamaterials

1. Introduction

The category of 'Extremal Materials' has been introduced in Milton and Cherkaev (1995) to define materials that at the same time show very soft and very stiff deformation modes (unimode, bimode, trimode, quadramode and pentamode materials, depending on the number of soft modes). Such a definition applies to a special class of mechanical metamaterials, i.e. composite materials, structural foams, pin-jointed trusses; cellular materials with re-entrant cells; rigid rotational elements: chiral lattices; etc., which feature special mechanical properties. The latter may include, e.g.: auxetic deformation modes; negative compressibility; negative stiffness phases; high composite stiffness and damping, to name just a few examples (cf.Lakes (1987); Milton (1992, 2002); Kadic et al. (2012); Spadoni and Ruzzene (2012); Nicolaou and Motter (2012); Milton (2013); Kochmann (2014), and references therein). Extremal materials are well suited to manufacture composites with enhanced toughness and shear strength (auxetic fiber reinforced composite); artificial blood vessels; energy absorption tools; and intelligent materials (cf. Liu (2006)). Rapid prototyping techniques for the manufacturing of materials with nearly pentamode behavior, and bistable elements with negative stiffness have been recently presented in Kadic et al. (2012) and Kashdan et al. (2012), respectively.

Email addresses: f.fraternali@unisa.it (F. Fraternali), gcarpentieri@unisa.it (G. Carpentieri), adamendola@gmail.com (A. Amendola)

Structural lattices are nowadays employed to manufacture phononic crystals and acoustic metamaterials, i.e., periodic arrays of particles/units, freestanding or embedded in in fluid or solid matrices with contrast in mass density and/or elastic moduli, eventually engineered with local resonant inclusions (Lu et al., 2009). Such artificial materials are designed to gain a variety of unusual acoustic behaviors, such as, e.g., phononic band-gaps; sound control; negative effective mass density; negative effective bulk modulus; negative effective refraction index; wave steering and directional behavior (cf. Liu et al. (2000); Li and Chan (2004); Ruzzene and Scarpa (2005); Daraio et al. (2006); Engheta and Ziolkowski (2006); Fang et al. (2006); Gonella and Ruzzene (2008); Lu et al. (2009); Zhang et al. (2009); Bigoni et al. (2013); Casadei and Rimoli (2013), and the references therein). Particularly interesting is the use of geometrical nonlinearities for the in situ tuning of phononic crystals (Bertoldi and Boyce, 2008; Wang et al., 2013); pattern transformation by elastic instability (Lee et al., 2012); as well as the optimal design of auxetic composites, and soft metamaterials incorporating fluids, gels and soft solid phases (Kochmann and Venturini, 2013; Brunet et al., 2013). Nonlinear metamaterials may support very compact compression solitary waves, in correspondence with a stiffening elastic response of the unit cells; or alternatively rarefaction pulses, when instead the unit cells exhibit a softening-type elastic behavior (cf. Friesecke and Matthies (2002); Fraternali et al. (2012); Nesterenko (2001); Herbold and Nesterenko (2013)).

This paper presents a mechanical study of the axial response of tensegrity prisms featuring large displacements, varying aspect ratios, prestress states, and material properties. We focus on the response of such structures under uniform axial loading, showing that they can exhibit extreme stiffening or, alternatively, extreme softening behavior, depending on suitable design variables. Interestingly, such a variegated mechanical response is a consequence of purely geometric nonlinearities. By extending the tensegrity prism models already in the literature (Oppenheim and Williams, 2000; Fraternali et al., 2012), we assume that the bases and bars of the tensegrity prism may show either elastic or rigid behavior. The presented models lead us to recover the extreme stiffening-type response in the presence of rigid bases already studied in Oppenheim and Williams (2000); Fraternali et al. (2012). In addition, we discover a new, extreme softening-type response. The latter is associated with a snap buckling phenomenon eventually leading to the complete axial collapse of the structure. We validate our theoretical and numerical results through comparisons with an experimental study on the quasi-static compression of physical models (Amendola et al., 2014). The extreme hard/soft behaviors of tensegrity prisms can be usefully exploited to manufacture metamaterials supporting special types of solitary waves, and 2D or 3D highly anisotropic systems including soft and hard units (Fraternali et al., 2012; Herbold and Nesterenko, 2013; Ruzzene and Scarpa, 2005; Casadei and Rimoli, 2013). The structure of this paper is as follows: in Section 2, we formulate a geometrically nonlinear model of a regular minimal tensegrity prism. Next, we present a collection of numerical results referring to tensegirity prisms with different aspect ratios, prestress states, and material properties (Section 3). In Section 4, we validate such results against compression tests on physical models. We end in Section 5 by drawing the main conclusions of the present study, and discussing future applications of tensegrity structures for the manufacture of innovative periodic lattices and metamaterials.

2. Geometrically nonlinear model of an axially loaded tensegrity prism

Let us consider an arbitrary configuration of a *regular minimal tensegrity prism* (Skelton and de Oliveira, 2010), which consists of two sets of *horizontal strings*: $1-2-3$ (*top strings*) and $4-5-6$ (*bottom strings*); three *cross strings*: 1-6, 2-4, and 3-5; and three *bars*: 1-4, 2-5, and 3-6 (Fig. 1). The horizontal strings form two equilateral triangles with side length ℓ, which are rotated with respect to each other by an arbitrary *angle of twist* φ. On introducing the Cartesian frame $\{O, x, y, z\}$ depicted in Fig. 1, which has the origin at the center of mass of the bottom base, we obtain the following expressions of the nodal coordinate vectors

$$\begin{aligned}
\mathbf{n}_1 &= \begin{bmatrix} \frac{\ell}{\sqrt{3}} \\ 0 \\ 0 \end{bmatrix}, \ \mathbf{n}_2 = \begin{bmatrix} -\frac{\ell}{2\sqrt{3}} \\ \frac{\ell}{2} \\ 0 \end{bmatrix}, \ \mathbf{n}_3 = \begin{bmatrix} -\frac{\ell}{2\sqrt{3}} \\ -\frac{\ell}{2} \\ 0 \end{bmatrix}, \ \mathbf{n}_4 = \begin{bmatrix} \frac{\ell\cos(\varphi)}{\sqrt{3}} \\ \frac{\ell\sin(\varphi)}{\sqrt{3}} \\ h \end{bmatrix}, \\
\mathbf{n}_5 &= \begin{bmatrix} -\frac{1}{2}\ell\sin(\varphi) - \frac{\ell\cos(\varphi)}{2\sqrt{3}} \\ \frac{1}{2}\ell\cos(\varphi) - \frac{\ell\sin(\varphi)}{2\sqrt{3}} \\ h \end{bmatrix}, \ \mathbf{n}_6 = \begin{bmatrix} \frac{1}{2}\ell\sin(\varphi) - \frac{\ell\cos(\varphi)}{2\sqrt{3}} \\ -\frac{\ell\sin(\varphi)}{2\sqrt{3}} - \frac{1}{2}\ell\cos(\varphi) \\ h \end{bmatrix}
\end{aligned} \tag{1}$$

with h denoting the *prism height*. The bars 1-4, 2-5, and 3-6 have the same length b, which is easily computed by

$$b = \sqrt{h^2 - \frac{2}{3}\ell^2\cos(\varphi) + \frac{2\ell^2}{3}} \tag{2}$$

while the cross strings 1-6, 2-4, and 3-5 have equal lengths s given by

$$s = \frac{\sqrt{3h^2 - \sqrt{3}\ell^2\sin(\varphi) + \ell^2\cos(\varphi) + 2\ell^2}}{\sqrt{3}} \tag{3}$$

We assume that the prism is loaded in the z direction by three equal forces (each of magnitude $f = F/3$) in correspondence with the bottom base $1, 2, 3$, and three forces of equal magnitude but opposite direction in correspondence with the top base $4, 5, 6$ (Fig. 1). Under such a uniform axial loading, it is easy to recognize that the deformation of the prism maintains its top and bottom bases parallel to each other, and simultaneously changes the angle of twist φ and the height h. The *geometrically feasible* configurations are obtained by letting φ vary between $\varphi = -\pi/3$ (cross-strings touching each other), and $\varphi = \pi$ (bars touching each other), as shown in Fig. 2. Hereafter, we refer to the configuration with the bars touching each other as the *'locking'* configuration of the prism. Let us consider the equilibrium equations associated with an arbitrary node of the prism,

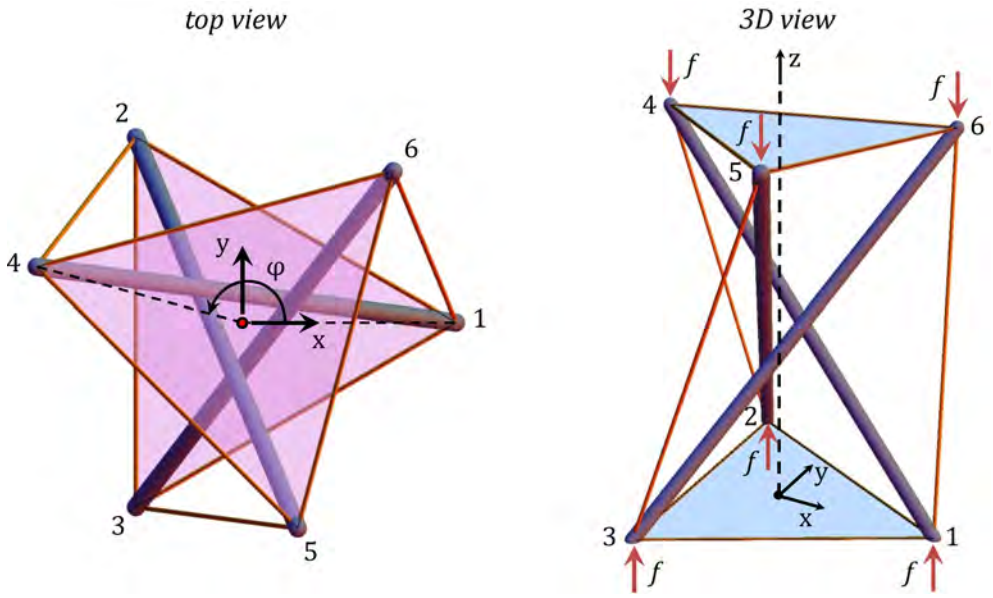

Figure 1: Reference configuration of a minimal regular tensegrity prism.

which set to zero the summation of all the forces acting on the given node in the current configuration. It is an easy task to show that such equations can be written as it follows

$$\begin{aligned}
\frac{1}{6}\ell\left(2\sqrt{3}(x_1+3x_2-x_3)+\sqrt{3}(x_1+2x_3)\cos(\varphi)-3x_1\sin(\varphi)\right) &= 0\\
\frac{1}{6}\ell\left(\sqrt{3}(x_1+2x_3)\sin(\varphi)+3x_1\cos(\varphi)\right) &= 0\\
h(x_3-x_1)-\frac{F}{3} &= 0
\end{aligned}\qquad (4)$$

where x_1, x_2 and x_3 are the forces per unit length (i.e, the *force densities*) acting in the cross-string, base-strings, and bar attached to the current node, respectively. Such force densities are assumed positive if the strings are stretched, and the bars are compressed. We say that the prism occupies a proper *tensegrity placement* if one has: $x_1 \geq 0, x_2 \geq 0$ (i.e., the strings are either in tension or, at most, slack). It is not difficult to verify that the system of equations (4) admits the following general solution

$$\begin{aligned}
x_1 &= -\frac{2F\sin(\varphi)}{3\sqrt{3}h\left(\sqrt{3}\sin(\varphi)+\cos(\varphi)\right)}\\
x_2 &= -\frac{F\left(\sin^2(\varphi)-\sqrt{3}\sin(\varphi)+\cos^2(\varphi)-\cos(\varphi)\right)}{9h\left(\sqrt{3}\sin(\varphi)+\cos(\varphi)\right)}\\
x_3 &= \frac{F}{3h}-\frac{2F\sin(\varphi)}{3\sqrt{3}h\left(\sqrt{3}\sin(\varphi)+\cos(\varphi)\right)}
\end{aligned}\qquad (5)$$

Restricting our attention to the geometrically feasible configurations ($\varphi \in [-\pi/3, \pi]$), we note that the solution (5) becomes indeterminate when either $\varphi = -\pi/6$, or $\varphi = 5\pi/6$,

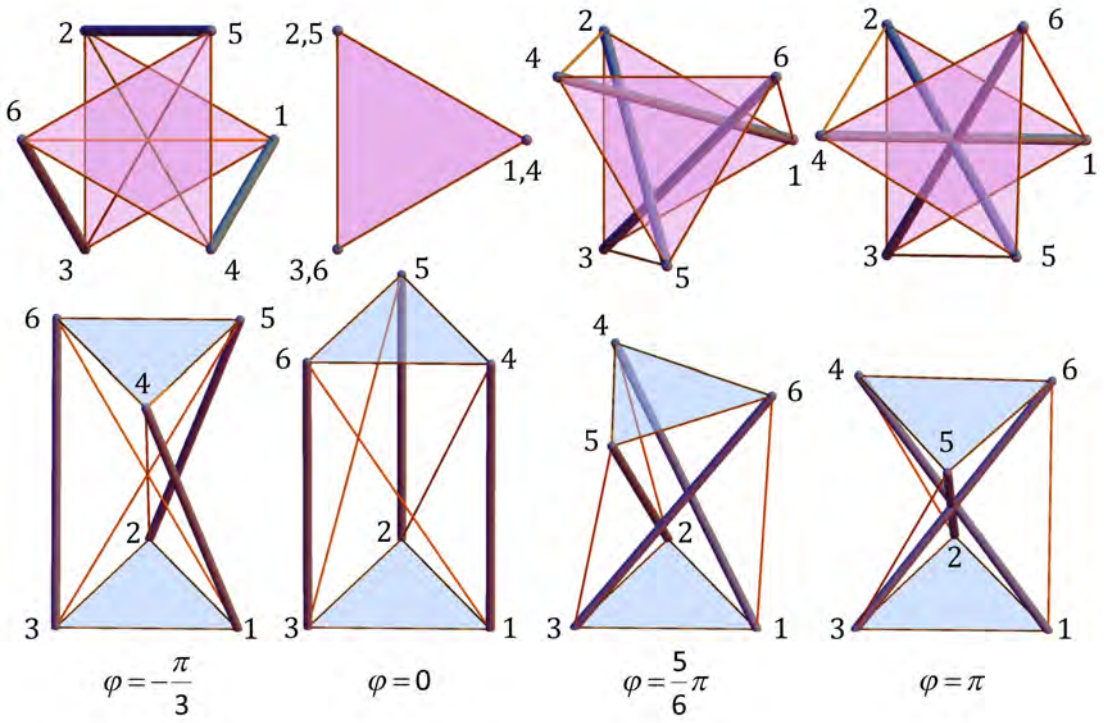

Figure 2: Sequence of configurations corresponding to feasible values of the twisting angle φ.

that is, when the quantity $\sqrt{3}\sin(\varphi)+\cos(\varphi)$ is zero. This means that the configurations corresponding to such values of φ may exhibit nontrivial states of self-stress, i.e., nonzero force densities in the prism members for $F = 0$ (*prestressable* configurations). By solving the first two equations (4) for x_2 and x_3, we characterize the self-stress states of the prism by

$$\varphi = -\frac{\pi}{6}: \quad x_2 = -\tfrac{x_1}{\sqrt{3}}, \quad x_3 = x_1 \tag{6}$$

$$\varphi = \frac{5}{6}\pi: \quad x_2 = \tfrac{x_1}{\sqrt{3}}, \quad x_3 = x_1 \tag{7}$$

for arbitrary x_1. Eqs. (6) and (7) show that a nontrivial state of self-stress compatible with an effective tensegrity placement is possible only for $\varphi = 5\pi/6$. As a matter of fact, Eq. (6) highlights that x_1 and x_2 have opposite signs for $\varphi = -\pi/6$, which implies that the prism is either unstressed ($x_1 = x_2 = x_3 = 0$), or has some strings stretched and the others compressed in such a configuration. In contrast, Eq. (7) reveals that x_1 and x_2 have equal signs for $\varphi = 5\pi/6$. The prism is loaded in compression for $\theta > 0$, and in tension for $\theta < 0$, where $\theta = \varphi - 5\pi/6$ (cf. Section 3, and Oppenheim and Williams (2000); Fraternali et al. (2012)). By manipulating Eqs. (1) and (5), we detect that all the cross strings are vertical and carry force densities $x_1 = f/h$, for $\varphi = 2/3\pi$ ($\theta = -\pi/6$). In the same configuration, the base strings and the bars carry zero forces ($x_2 = x_3 = 0$).

We take as a *reference* the configuration of the prism such that $\varphi = \varphi_0 = 5\pi/6$, and let s_0, ℓ_0 and b_0 denote the lengths of the cross-strings, base-strings and bars in such a configuration, respectively. By inserting ℓ_0 and s_0 into Eqs. (2) and (3), we can easily compute the reference values of the prism height and bar length as follows

$$h_0 \;=\; \sqrt{s_0^2 + \frac{1}{3}\left(\sqrt{3}-2\right)\ell_0^2}, \qquad b_0 \;=\; \sqrt{s_0^2 + \frac{2\ell_0^2}{\sqrt{3}}} \tag{8}$$

2.1. Fully elastic model

A *fully elastic model* is obtained by describing all the prism members (bars and strings) as linear springs characterized by the following constitutive laws (Skelton and de Oliveira, 2010)

$$x_1 \;=\; \frac{1}{s}\,k_1\,(s - s_N), \quad x_2 \;=\; \frac{1}{\ell}\,k_2\,(\ell - \ell_N), \quad x_3 \;=\; -\,\frac{1}{b}\,k_3\,(b - b_N) \tag{9}$$

where k_1, k_2 and k_3 are spring constants, and s_N, ℓ_N and b_N are the *rest lengths* (or *natural lengths*) of cross-strings, base-strings and bars, respectively. Upon neglecting the change of the cross-section areas of all members during the prism deformation, we compute the spring constants as follows (Skelton and de Oliveira, 2010)

$$k_1 \;=\; \frac{E_1 A_1}{s_N}, \quad k_2 \;=\; \frac{E_2 A_2}{\ell_N}, \quad k_3 \;=\; \frac{E_3 A_3}{b_N} \tag{10}$$

where E_1, E_2, E_3, and A_1, A_2, A_3 are the elastic moduli and the cross-section areas of the cross-strings, base-strings and bars, respectively.

2.1.1. Reference configuration

Hereafter, we assume that ℓ_N and s_N are given, and that the cross-string *prestrain* is prescribed, i.e., the quantity

$$p_0 \;= (s_0 - s_N)/s_N \tag{11}$$

In line with the above assumptions, we compute the reference length of the cross-strings (s_0), and the reference value of the force density in such members ($x_1^{(0)}$) through

$$s_0 \;=\; s_N(1 + p_0) \tag{12}$$

$$x_1^{(0)} \;=\; \frac{1}{s_0}\,k_1\,(s_0 - s_N) \;=\; \frac{A_1 E_1}{s_N}\,\frac{p_0}{1+p_0}, \tag{13}$$

Using (7), (9) and (13), we are led to the following reference values of the force densities in the base strings ($x_2^{(0)}$) and bars ($x_3^{(0)}$)

$$x_2^{(0)} \;=\; \frac{1}{\ell_0}\; k_2\; (\ell_0 - \ell_N) \;=\; \frac{A_1 E_1}{\sqrt{3} s_N}\; \frac{p_0}{1+p_0} \tag{14}$$

$$x_3^{(0)} \;=\; -\;\frac{1}{b_0}\; k_3\; (b_0 - b_N) \;=\; \frac{A_1 E_1}{s_N}\; \frac{p_0}{1+p_0} \tag{15}$$

Eq. (14) can be solved for ℓ_0, yielding

$$\ell_0 \;=\; \frac{3 A_2 E_2\, (p_0+1)\, s_N \ell_N}{p_0 \left(3 A_2 E_2 s_N - \sqrt{3} A_1 E_1 \ell_N\right) + 3 A_2 E_2 s_N} \tag{16}$$

On the other hand, the substitution of (12) and (16) into $(8)_2$ gives

$$b_0 \;=\; \eta\; s_0 \;=\; \eta\; (1+p_0)\; s_N \tag{17}$$

where

$$\psi \;=\; \sqrt{\frac{6\sqrt{3} A_2^2 E_2^2 \ell_N^2}{\left(p_0 \left(3 A_2 E_2 s_N - \sqrt{3} A_1 E_1 \ell_N\right) + 3 A_2 E_2 s_N\right)^2} + 1} \tag{18}$$

By solving Eq. (15) for b_N and employing (17), we finally obtain

$$b_N \;=\; \frac{\psi A_3 E_3}{A_3 E_3 - \psi A_1 E_1}\; (1+p_0)\; s_N \tag{19}$$

2.1.2. The elastic problem

The substitution of Eqns. (9) into (4) leads us to the following elastic problem

$$\begin{aligned} g_1 \;=\; \frac{1}{6}\ell \Bigg(& k_3\; 4\sin^2\left(\frac{\varphi}{2}\right) \left(\sqrt{3} - \frac{3 b_N}{\sqrt{3h^2 - 2\ell^2\cos(\varphi) + 2\ell^2}}\right) \\ & +\; k_1\; \left(-3\sin(\varphi) + \sqrt{3}\cos(\varphi) + 2\sqrt{3}\right) \;+\; k_2\; \frac{6\sqrt{3}\,(\ell - \ell_N)}{\ell} \\ & -\; k_1\; \frac{3 s_N \left(-\sqrt{3}\sin(\varphi) + \cos(\varphi) + 2\right)}{\sqrt{3h^2 - \sqrt{3}\ell^2\sin(\varphi) + \ell^2\cos(\varphi) + 2\ell^2}} \Bigg) \;=\; 0 \end{aligned} \tag{20}$$

$$\begin{aligned} g_2 \;=\; \frac{1}{6}\ell \Bigg(& k_3\; 2\sin(\varphi) \left(\frac{3 b_N}{\sqrt{3h^2 - 2\ell^2\cos(\varphi) + 2\ell^2}} - \sqrt{3}\right) \\ & +\; k_1\; \left(\sqrt{3}\sin(\varphi) + 3\cos(\varphi)\right) \\ & -\; k_1\; \frac{3 s_N \left(\sin(\varphi) + \sqrt{3}\cos(\varphi)\right)}{\sqrt{3h^2 - \sqrt{3}\ell^2\sin(\varphi) + \ell^2\cos(\varphi) + 2\ell^2}} \Bigg) \;=\; 0 \end{aligned} \tag{21}$$

$$g_3 \;=\; -f \;+\; k_3\, h \left(\frac{b_N}{\sqrt{h^2 - \frac{2}{3}\ell^2 \cos(\varphi) + \frac{2\ell^2}{3}}} - 1 \right)$$
$$+\; k_1\, h \left(\frac{\sqrt{3} s_N}{\sqrt{3h^2 - \sqrt{3}\ell^2 \sin(\varphi) + \ell^2 \cos(\varphi) + 2\ell^2}} - 1 \right) \;=\; 0 \qquad (22)$$

2.1.3. Path-following method

We formulate a path-following approach to the nonlinear problem (20)–(22), by introducing the following 'extended system' (Riks, 1984; Wriggers and Simo, 1990)

$$\tilde{\mathbf{g}} \;=\; \begin{bmatrix} \mathbf{g}(\mathbf{v}, f) \\ \\ \psi(\mathbf{v}, f) \end{bmatrix} = 0 \qquad (23)$$

where we set $\mathbf{v} = [\ell, \varphi, h]^T$, $\mathbf{g} = [g_1, g_2, g_3]^T$, and let $\psi(\mathbf{v}, f) = 0$ denote a constraint equation characterizing the given loading condition. In the case of a displacement control loading, we in particular assume

$$\psi \;=\; v_k - c = 0, \qquad (24)$$

letting v_k coincide with $v_1 \equiv \ell$ (*base edge control*); $v_2 \equiv \varphi$ (*twist control*) or $v_3 \equiv h$ (*height control*), and letting c denote a given constant. The Newton–Raphson linearization of (23) at a given starting point $(\bar{\mathbf{v}},\, \bar{f})$ leads us to the incremental problem

$$\begin{bmatrix} \nabla_{\mathbf{v}}\mathbf{g} & \nabla_f \mathbf{g} \\ \\ \nabla_{\mathbf{v}}\psi^T & \nabla_f \psi \end{bmatrix} \begin{bmatrix} \Delta\mathbf{v} \\ \\ \Delta f \end{bmatrix} = - \begin{bmatrix} \bar{\mathbf{g}} \\ \\ \bar{\psi} \end{bmatrix} \qquad (25)$$

where we set $\bar{\mathbf{g}} = \mathbf{g}(\bar{\mathbf{v}}, \bar{f})$; $\bar{\psi} = \psi(\bar{\mathbf{v}}, \bar{f})$; and

$$\nabla_{\mathbf{v}}\mathbf{g} = \begin{bmatrix} \frac{\partial g_1}{\partial v_1} & \frac{\partial g_1}{\partial v_2} & \frac{\partial g_1}{\partial v_3} \\ \\ \frac{\partial g_2}{\partial v_1} & \frac{\partial g_2}{\partial v_2} & \frac{\partial g_2}{\partial v_3} \\ \\ \frac{\partial g_3}{\partial v_1} & \frac{\partial g_3}{\partial v_2} & \frac{\partial g_3}{\partial v_3} \end{bmatrix}, \quad \nabla_f \mathbf{g} = \begin{bmatrix} \frac{\partial g_1}{\partial f} \\ \\ \frac{\partial g_2}{\partial f} \\ \\ \frac{\partial g_3}{\partial f} \end{bmatrix}, \quad \nabla_{\mathbf{v}}\psi = \begin{bmatrix} \frac{\partial \Psi}{\partial \mathbf{v}_1} \\ \\ \frac{\partial \Psi}{\partial \mathbf{v}_1} \\ \\ \frac{\partial \Psi}{\partial \mathbf{v}_1} \end{bmatrix} \qquad (26)$$

We now introduce the notations $\mathbf{V} := \nabla_{\mathbf{v}}\mathbf{g}$ and $\mathbf{f} := \nabla_f \mathbf{g} = [0, 0, -1]^T$, and assume that $\mathbf{V}$ is invertible at $(\mathbf{v} = \bar{\mathbf{v}},\, f = \bar{f})$. The incremental problem (25) is solved by first computing the partial solutions

$$\Delta\mathbf{v}_f \;=\; -\mathbf{V}^{-1}\mathbf{f} \;=\; \begin{bmatrix} V_{13}^{-1} \\ V_{23}^{-1} \\ V_{33}^{-1} \end{bmatrix}, \qquad \Delta\mathbf{v}_g \;=\; -\mathbf{V}^{-1}\bar{\mathbf{g}}, \qquad (27)$$

and next the updates

$$\Delta\mathbf{v} = \Delta f \Delta\mathbf{v}_f + \Delta\mathbf{v}_g, \tag{28}$$

$$\Delta f = -\frac{\bar{\psi} + \nabla_{\mathbf{v}}\psi \cdot \Delta\mathbf{v}_g}{\nabla_f\psi + \nabla_{\mathbf{v}}\psi \cdot \Delta\mathbf{v}_f} \tag{29}$$

Equations (28)–(29) lead us to the new predictor $(\bar{\mathbf{v}} + \Delta\mathbf{v},\ \bar{f} + \Delta f)$, which is used to reiterate the updates (28)–(29), until the residual $\left\|\mathbf{g}(\bar{\mathbf{v}}, \bar{f})\right\|$ gets lower than a given tolerance. Once a new equilibrium point is obtained, the value of constant c in Eqn. (24) is updated and the path-following procedure is continued. The explicit expression for the $\mathbf{V}$ matrix is given in Appendix.

Let us assume $\psi = h - \bar{h}$ (height control loading). By writing Eqn. (28) in correspondence with a solution of the extended system (23) ($\bar{\mathbf{g}} = \mathbf{0}$, $\bar{\psi} = 0$), we easily obtain $\Delta\mathbf{v}_g = 0$, and

$$\begin{bmatrix}\Delta\ell\\ \Delta\varphi\\ \Delta h\end{bmatrix} = \Delta f \begin{bmatrix}V_{13}^{-1}\\ V_{23}^{-1}\\ V_{33}^{-1}\end{bmatrix} \tag{30}$$

which implies

$$\Delta h = \Delta f\ V_{33}^{-1} = \frac{\Delta F}{3}\ V_{33}^{-1} \tag{31}$$

Eqn. (31) shows that the *axial stiffness* K_h^{el} of the fully elastic model is given by

$$K_h^{el} = -\frac{3}{V_{33}^{-1}} \tag{32}$$

In the Supplementary Data, we give the the analytic expression of K_h, which is rather cumbersome. The value of such a quantity at $\mathbf{v} = \mathbf{v}_0 = [\ell_0, \varphi_0, h_0]^T$ defines the axial stiffness $K_{h_0}^{el}$ of the elastic prism in correspondence with the reference configuration. It is not difficult to show that it results in (see Supplementary Data)

$$\begin{aligned} K_{h_0}^{el} = {} & \frac{p_0}{1+p_0}\left\{36k_1\eta_0^2\left((3+2\sqrt{3}+\sqrt{3}\eta_0^2)k_1k_2 + (-2+\sqrt{3}-\eta_0^2)k_1k_1\frac{p_0}{1+p_0}\right.\right. \\ & -6k_2k_1\frac{p_0}{1+p_0} + k_3(2\sqrt{3}k_1 + (-3+2\sqrt{3}+\sqrt{3}\eta_0^2)k_2 - (2+\sqrt{3}+\eta_0^2) \\ & \left.\left.\times k_1\frac{p_0}{1+p_0})\right)\right\} / \left\{6k_1\frac{p_0}{1+p_0}\left(\sqrt{3}(1+8\eta_0^2+2\eta_0^4)k_2 - 2\eta_0^4k_1\frac{p_0}{1+p_0}\right)\right. \\ & +k_1\Big(3(2+\sqrt{3}+\eta_0^2)k_2 + (-3+2\sqrt{3}+(-24+13\sqrt{3})\eta_0^2)k_1\frac{p_0}{1+p_0}\Big) \\ & \left.+k_3\Big(6k_1 + 3(2-\sqrt{3}+\eta_0^2)k_2 + (3+2\sqrt{3}+(24+13\sqrt{3})\eta_0^2)k_1\frac{p_0}{1+p_0}\Big)\right\} \end{aligned} \tag{33}$$

where η_0 denotes the following aspect ratio

$$\eta_0 = \frac{h_0}{a_0} \tag{34}$$

Equation (33) highlights that $K_{h_0}^{el}$ is zero for $p_0 = 0$, and that the quantity $(\ell_0 - \ell_N)/\ell_0 = p_0/(1+p_0)$ can be used to characterize the state of prestress of the structure in place of p_0 (Micheletti, 2013).

2.2. Rigid-elastic model

In a series of studies available in the literature, the mechanical response of tensegrity prisms has been analyzed by assuming that the bases and bars behave rigidly, while the cross strings respond as elastic springs (*rigid-elastic model*, cf., e.g., Oppenheim and Williams (2000); Fraternali et al. (2012)). Such a modeling keeps b and ℓ fixed ($b = b_0 =$ const, $\ell = \ell_0 =$ const), and relates h to φ through Eq. (2). Let us solve Eq. (2) for h, obtaining the equation

$$h = \sqrt{b^2 - \frac{2}{3}\ell^2(1-\cos\varphi)} \tag{35}$$

which, once inverted (for $-\pi/3 \leq \varphi \leq \pi$), gives

$$\varphi = \arccos\left(1 - \frac{b^2-h^2}{2a^2}\right) \tag{36}$$

where $a = \ell/\sqrt{3}$ denoted the radius of the circumference circumscribed to the base triangles. The response of the rigid–elastic model is easily modeled by substituting $(9)_1$ into the equilibrium equations (4), and solving the resulting system of algebraic equations with respect to F, x_2, and x_3, for given h (or φ). It is not difficult to verify that such an approach leads to the same constitutive law given in Oppenheim and Williams (2000); Fraternali et al. (2012), that is

$$\begin{aligned} F &= 3k_1\,(s-s_N)\,\frac{h}{2s}\left(3+\frac{\sqrt{3}\,(2a^2+h^2-b^2)}{a^2\sqrt{-\frac{(h^2-b^2)(4a^2+h^2-b^2)}{a^4}}}\right) \\ &= \frac{k_1\csc(\varphi)\left(3\sin(\varphi)+\sqrt{3}\cos(\varphi)\right)\sqrt{3b^2+2\ell^2\cos(\varphi)-2\ell^2}}{2\sqrt{3b^2-\sqrt{3}\ell^2\sin(\varphi)+3\ell^2\cos(\varphi)}} \\ &\quad\times\left(\sqrt{9b^2-3\sqrt{3}\ell^2\sin(\varphi)+9\ell^2\cos(\varphi)}-3s_N\right) \end{aligned} \tag{37}$$

It is easily shown that the rigid–elastic model predicts a progressively stiffening response under increasing axial strains, with the exception of extremely 'thick geometries

(cf. Sect. 3.3). Once h (or φ) is given, x_1 is computed through $(9)_1$ and (3); F is computed through (37); and x_2 and x_3 are obtained from the equilibrium equations (4). The differentiation of (37) with respect to h gives the tangent axial stiffness of the present model (see Supplementary Data). The reference value of such a quantity ($\varphi = 5/6\pi$) is given by

$$K_{h_0}^{rigel} \;=\; -F'(h = h_0) \;=\; 12\,\sqrt{3}\,k_1 \frac{p_0}{1+p_0}\,\eta_0^2 \tag{38}$$

and it is immediately seen that also K_0^{rigel} is zero for $p_0 = 0$, as well as K_0^{el} (cf. also Supplementary Data).

3. Numerical results

The current section presents a collection of numerical results aimed to illustrate the main features of the mechanical models presented in Section 2. We examine the mechanical response of tensegrity prisms having the same features as the physical models studied in Amendola et al. (2014). Such prisms are equipped with M8 threaded bars made out of white zinc plated grade 8.8 steel (DIN 976-1), and strings consisting of PowerPro® braided Spectra® fibers with 0.76 mm diameter (commercialized by Shimano American Corporation - Irvine CA). The properties of the employed materials are shown in Table 1. Let $\bar{A}_1$, $\bar{A}_2$, $\bar{A}_3$ and $\bar{E}_1$, $\bar{E}_2$, $\bar{E}_3$ denote the cross-sectional areas and elastic moduli of the strings and bars defined according to Table 1. In order to study the transition from the elastic to the rigid–elastic model, we hereafter study the mechanical response of elastic prisms endowed with the following spring constants (cf. Section 2.1).

$$k_1 \;=\; \frac{\bar{E}_1\bar{A}_1}{s_N}, \quad k_2 \;=\; \alpha\,\frac{\bar{E}_2\bar{A}_2}{\ell_N}, \quad k_3 \;=\; \beta\,\frac{\bar{E}_3\bar{A}_3}{b_N} \tag{39}$$

where α and β are rigidity multipliers ranging within the interval $[1, \infty]$. The case of $\alpha = \beta = 1$ corresponds to the fully elastic ('el') model of Sect. 2.1.2, while the limiting case with $\alpha = \beta \to \infty$ corresponds to the rigid–elastic ('rigel') model presented in Sect. 2.2. The equilibrium configurations of the elastic prism model are numerically determined through the path-following method given in Section 2.1.3, letting the angle of twist φ to vary within the interval $[2/3\pi, \pi)$, which corresponds to effective tensegrity placements of the structure (cf. Section 2). We examine a large variety of prestrains p_0, and both *thick* and *slender* reference configurations (cf. Figs. 3 and 9, respectively). Let $\delta = h_0 - h$ denote the axial displacement of the prism from the reference configuration, and let $\varepsilon = \delta/h_0$ denote the corresponding axial strain (positive when the prism is compressed). We name *stiffening* a branch of the $F - \delta$ response showing axial stiffness K_h increasing with $|\delta|$ (or $|\varepsilon|$), and *softening* a branch that instead shows K_h decreasing with $|\delta|$ ($|\varepsilon|$). The axial forces carried by the cross-strings, base-strings, and bars are denoted by N_1, N_2, and N_3, respectively. We assume that N_1 and N_2 are positive in tension, and that N_3 is instead positive in compression.

Property	bars	strings
area (mm^2)	36.6	0.45
mass density (kg/m^3)	7850	793
elastic modulus (GPa)	203.53	5.48

Table 1: Properties of the materials employed in the numerical simulations.

3.1. Thick prism model

We hereafter name 'thick' the mechanical model of a prism featuring: $s_N = 0.08$ m, $\ell_N = 0.132$ m, and reference lengths s_0, ℓ_0, b_0, and h_0 variable with the cross string prestrain p_0 (cf. Section 2.1.1). Table 2 shows noticeable values of such variables and K_{h_0}, for different prestrains p_0; the fully elastic model; and the rigid–elastic model presented in Sect. 2. It is seen that h_0 is always smaller than ℓ_0 in the present case, which justifies the name 'thick' given to the model under consideration. The difference between $K_{h_0}^{el}$ and $K_{h_0}^{rigel}$ grows with the prestrain p_0, being zero for $p_0 = 0$ ($K_{h_0}^{el} = K_{h_0}^{rigel} = 0$). Fig. 4 shows the force F vs. δ curves of the 'el' samples for different values of p_0. Fig. 5 provides the same curves for different values of the stiffness multipliers α and β, and $p_0 = 0.1$. Finally, Figs. 6 and 7 illustrate the variations with the angle of twist φ of the axial stiffness K_h; the prism height h; and the axial forces N_1, N_2 and N_3. In the 'el' case, the results in Figs. 4 and 6 highlight that the compressive response for $p_0 \leq 0.005$ initially features a stiffening branch, next a softening branch, and finally an unstable phase (F decreasing with δ), as the axial strain ε increases. When p_0 grows above 0.005, the initial stiffening branch disappears, and the compressive response is always softening. The final unstable branch is associated with the snap buckling of the prism to the completely collapsed configuration featuring zero height h (cf. Fig. 8). Such a collapse event can fully take place when $p_0 \geq 0.05$, but is instead prevented by prism locking for lower values of p_0 (Figs. 4 and 6). It is worth noting that the maximum compression displacement δ^{max} increases with p_0. For what concerns the tensile response, we observe that the 'el' model is always stiffening in tension, for any $p_0 \in [0, 0.4]$ (Figs. 4, 6). We also observe that the minimum axial displacement δ^{min} (i.e. the value of δ for $\varphi = 2/3\pi$) grows in magnitude with p_0.

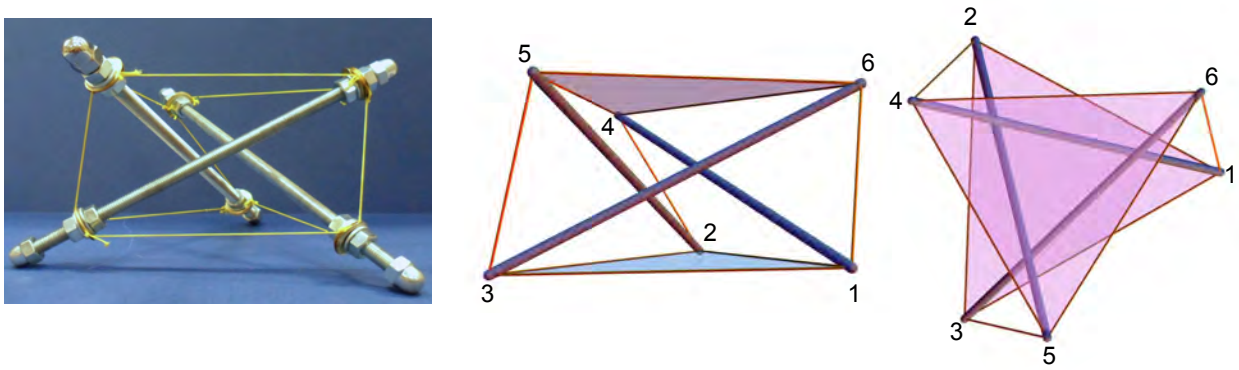

Figure 3: Thick prism model. Left: photograph of a real-scale example (Amendola et al., 2014). Center and right: 3D view (center) and top view (right) of the geometric model.

α=β	p_0	s_N (m)	s_0 (m)	ℓ_N (m)	ℓ_0 (m)	b_N (m)	b_0 (m)	h_0 (m)	K_{h_0} (MN/m)
1	0	0.080	0.0800	0.1320	0.1320	0.1628	0.1628	0.0696	0.0000
1	0.005	0.080	0.0804	0.1320	0.1326	0.1636	0.1636	0.0700	0.0026
1	0.1	0.080	0.0880	0.1320	0.1445	0.1785	0.1785	0.0767	0.0297
1	0.2	0.080	0.0960	0.1320	0.1569	0.1941	0.1940	0.0838	0.0393
1	0.3	0.080	0.1040	0.1320	0.1692	0.2095	0.2095	0.0909	0.0426
1	0.4	0.080	0.1120	0.1320	0.1814	0.2248	0.2248	0.0980	0.0435
$\to \infty$	0	0.080	0.0800	0.1320	0.1320	0.1628	0.1628	0.0696	0.0000
$\to \infty$	0.005	0.080	0.0804	0.1320	0.1320	0.1630	0.1630	0.0701	0.0027
$\to \infty$	0.1	0.080	0.0880	0.1320	0.1320	0.1669	0.1669	0.0787	0.0496
$\to \infty$	0.2	0.080	0.0960	0.1320	0.1320	0.1713	0.1713	0.0875	0.0920
$\to \infty$	0.3	0.080	0.1040	0.1320	0.1320	0.1759	0.1759	0.0962	0.1290
$\to \infty$	0.4	0.080	0.1120	0.1320	0.1320	0.1807	0.1807	0.1048	0.1617

Table 2: Geometric variables and initial axial stiffness K_{h_0} of the thick prism model, for different values of the cross-string prestrain p_0; the fully elastic model ($\alpha = \beta = 1$); and the rigid–elastic model ($\alpha = \beta \to +\infty$).

Let us now pass to studying the response of the thick prism model for different values of the rigidity multipliers α and β. The $F - \delta$ curves in Fig. 5 show that the response in compression of such a model switches from extremely soft to extremely stiff when α and β grow from 1 ('el' model) to $+\infty$ ('rigel' model). In particular, we observe that α (i.e., the base rigidity) plays a more substantial role in the mechanical response of such structures than does β (the bar rigidity multiplier). We indeed note that the $F-\delta$ curves for $\alpha = \beta = 10$ and $\alpha = \beta = 100$ are not much different from those corresponding to $\alpha = 10,\ \beta = 1$ and $\alpha = 100,\ \beta = 1$, respectively. This is due to the fact that the axial stiffness of the bars is much higher than the axial stiffness of the strings (cf. Table 1), which implies that the assumption of bar rigidity is more realistic than the assumption of base rigidity, in the present case. When $p_0 = 0.005$, Fig. 7 shows that the response in tension of the current prism is always stiffening, for all the examined values of α and β. In contrast, for $p_0 = 0.4$ we observe that such a response progressively switches from

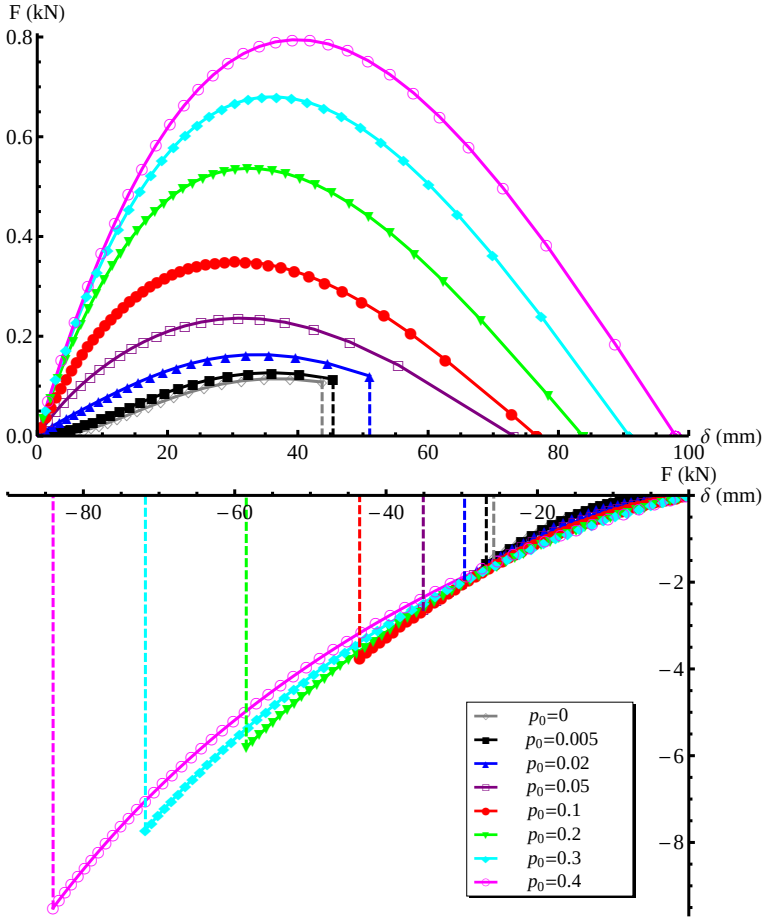

Figure 4: F–δ curves of the thick prism model, when loaded in compression (top), and tension (bottom), for $\alpha = \beta = 1$ and different values of p_0.

stiffening to softening, as α and β grow to infinity (Fig. 7). Overall, we note that the stroke of the prism ($\delta^{max} - \delta^{min}$) decreases with α and β (Fig. 5), and increases with p_0 (Fig. 4). Conversely, the value of K_h at $\delta = \delta^{max}$ increases with α and β (Fig. 7), and decreases with p_0 (Fig. 6).

The results in Fig. 6 highlight that the unstable phases of the 'el' model are associated with a progressive decrease of the force acting in the cross-strings (N_1). The decrease of N_1 with φ for $\alpha = \beta = 1$ is confirmed by the results given in Fig 7, which show that the cross-strings tend to become slack as φ approaches π ($\delta \to \delta^{max}$), in the 'el' case. The N_2 vs. φ curves of the base-strings highlight that N_2 grows monotonically with φ (starting with the value $N_2 = 0$ at $\varphi = 2/3\pi$), independently of p_0, α and β (Figs. 6 and 7). In particular, the rate of growth of N_2 decreases with p_0, and increases with α and β, tending to infinity for $\varphi \to \pi$ ($\delta \to \delta^{max}$), when $\alpha = \beta \to \infty$. This implies that, in real life, the base strings would yield before reaching the 'locking' configuration, in the 'rigel' limit. The axial force response of the bars resembles that of the base strings, and we note that the bars tend to buckle before reaching the locking configuration in the'rigel' limit. For $p_0 \geq 0.05$, it is worth noting that the maximum value of φ is less than π (cf. Figs. 6,

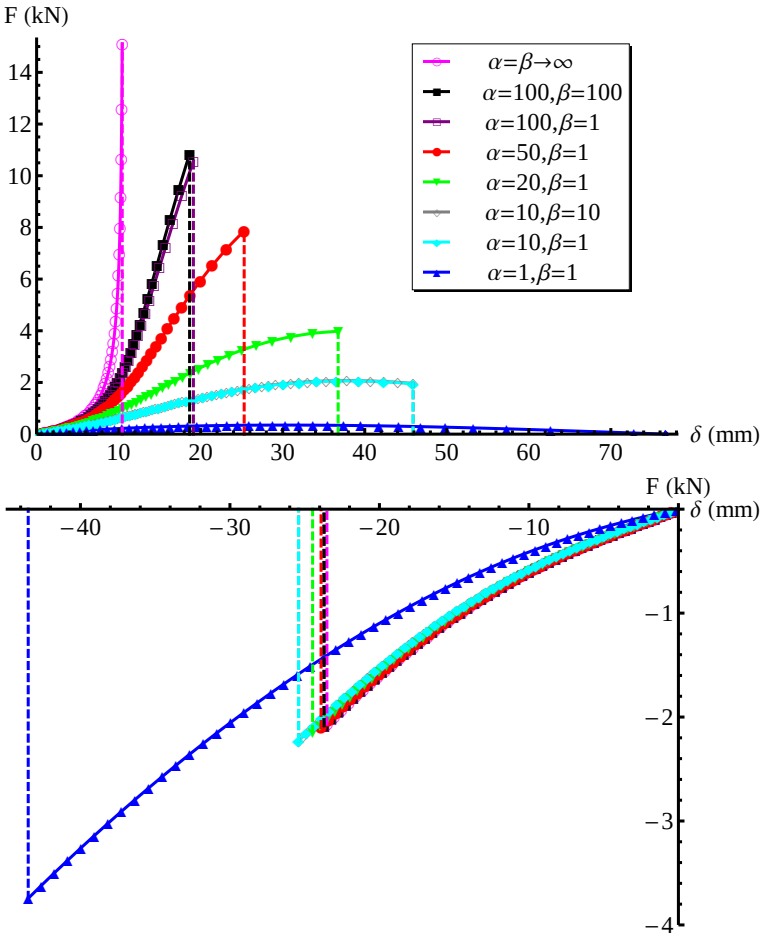

Figure 5: F–δ curves of the thick prism model, when loaded in compression (top), and tension (bottom), for $p_0 = 0.1$ and different values of α and β.

7), since in such cases the axial collapse precedes the locking configuration $\varphi = \pi$.

3.2. Slender prism model

The 'slender' prism model analyzed in the present study features: $s_N = 0.162$ m, $\ell_N = 0.08$ m, and height about twice the base side in the reference configuration (cf. Table 3). Figs. 10 and 11 show the force F vs. δ curves of such prisms for different values of p_0, α and β (see Supplementary Data for additional results). Some snapshots of the deformation history of the slender prism model for $\varphi \in [2/3\pi, \pi]$; $\alpha = \beta = 1$; and $p_0 = 0.4$ are illustrated in Fig. 12.

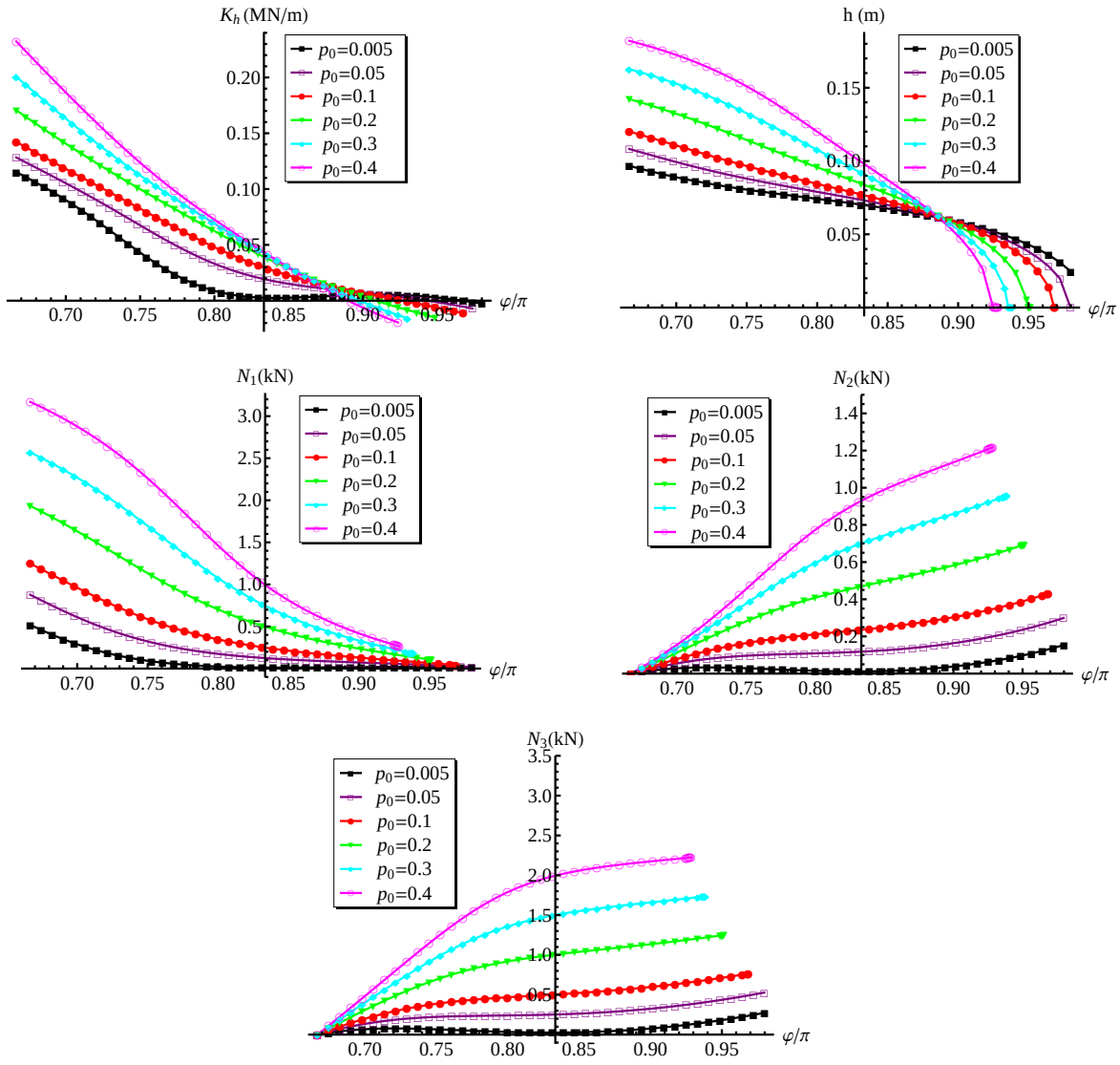

Figure 6: K_h vs. φ, h vs. φ, and N_1, N_2, N_3 vs. φ curves of the thick prism model for $\alpha = \beta = 1$, and different values of p_0.

In the 'el' model with $p_0 \leq 0.3$, we observe that the compressive response first shows a stiffening branch, and next a softening branch (cf. Fig. 10 and Supplementary Data). For $p_0 = 0.4$, the compressive branch of the F vs. δ (or F vs. φ) response is instead always softening, and terminates with an unstable phase. Fig. 10 also shows that the tensile response of the current prism is slightly softening for $p_0 \geq 0.1$. In contrast, for $p_0 \leq 0.05$ the same response is instead slightly stiffening. It is worth noting that the above behaviors are markedly different from those exhibited by the thick prism model analyzed in Section 3.1, since the latter feature unstable response in compression under low prestrains p_0, and always stiffening response in tension (Figs. 4, 6, 8). We now pass to examining the axial response of the slender prism model for different values of the stiffness multipliers α and β, and $p_0 = 0.1$. Fig. 11 shows that the compressive response for $p_0 = 0.1$ is almost linear when $\delta \to \delta^{max}$ in the 'el' case, and tends to get infinitely

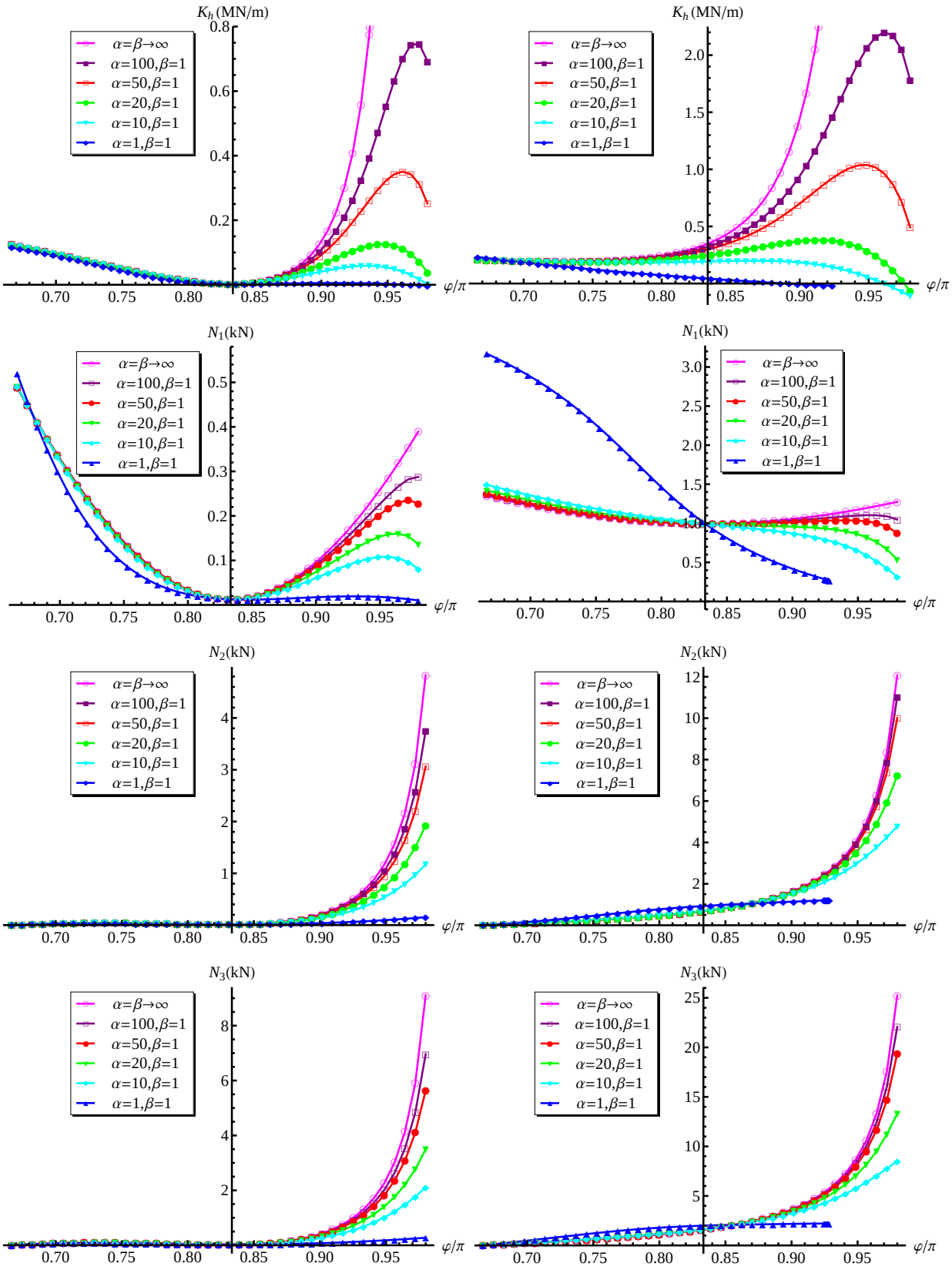

Figure 7: K_h vs. φ and N_1, N_2, N_3 vs. φ curves of the thick prism model for $p_0 = 0.005$ (left), $p_0 = 0.4$ (right), and different values of α and β.

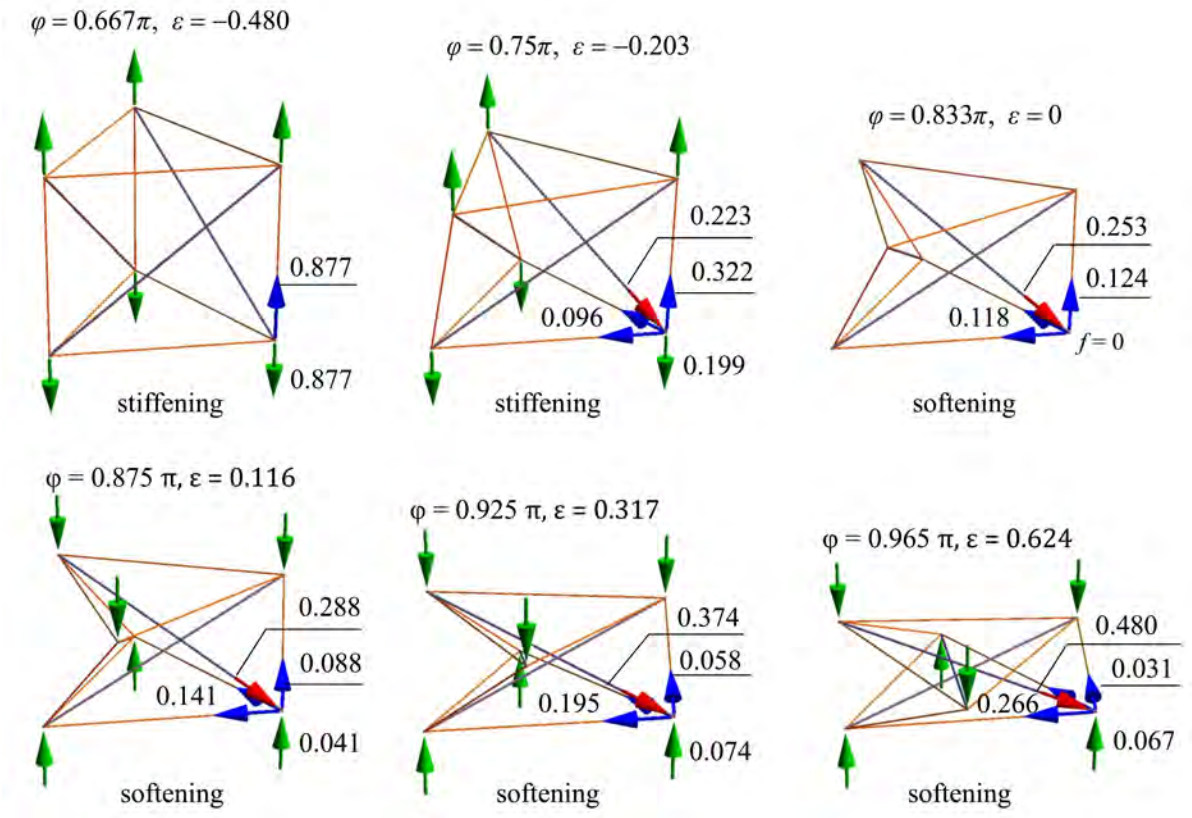

Figure 8: Member forces (kN) in different configurations of the thick prism model, for $\alpha = \beta = 1$, and $p_0 = 0.05$.

stiff in the 'rigel' limit. The tensile response is instead less sensitive to α and β, and always softening (Fig. 11). The individual responses of the prism members highlight that the softening response in compression is always associated with decreasing values of the force carried by the cross-strings, as in the case of the thick prism model examined in the previous section (cf. Supplementary Data). The deformation history illustrated in Fig. 12 highlights a marked stretching of the base-strings, in proximity to the locking configuration $\varphi = \pi$, when there results $\alpha = \beta = 1$, and $p_0 = 0.4$.

3.3. Prisms with arbitrary aspect ratio

The nature of the axial response of a generic prism can be predicted by computing the derivative of K_h with respect to h along the equilibrium path, that is, the quantity $H_h = dK_h/dh$. It is straightforward to realize that stiffening and softening behaviors correspond to $H_h < 0$ (i.e., $dK_h/d\delta > 0$), and $H_h > 0$ ($dK_h/d\delta < 0$), respectively. Making use of the results presented in Sect. 2.1.3, we get

$$\begin{aligned} H_h &= \frac{\partial K_h}{\partial h} + \frac{\partial K_h}{\partial \ell}\frac{\partial \ell}{\partial h} + \frac{\partial K_h}{\partial \varphi}\frac{\partial \varphi}{\partial h} \\ &= \frac{\partial K_h}{\partial h} + \frac{V_{13}^{-1}}{V_{33}^{-1}}\frac{\partial K_h}{\partial \ell} + \frac{V_{23}^{-1}}{V_{33}^{-1}}\frac{\partial K_h}{\partial \varphi} \end{aligned} \tag{40}$$

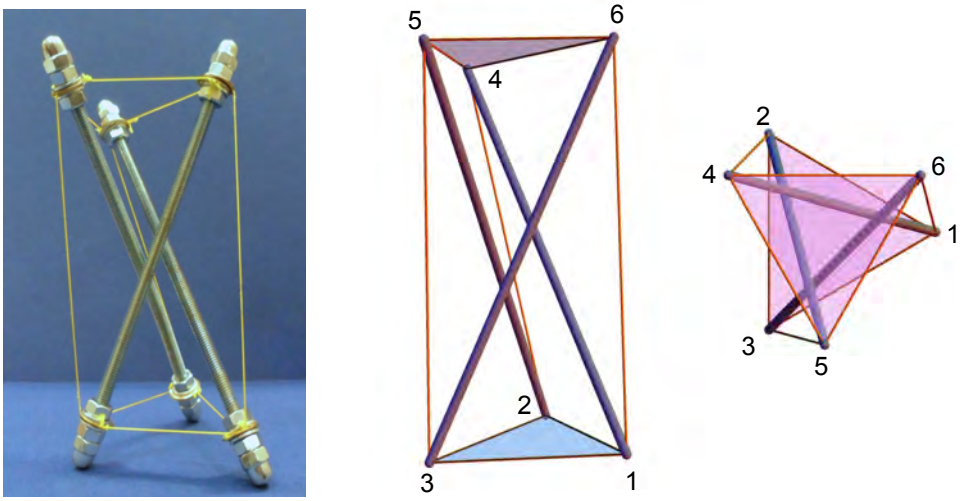

Figure 9: Slender prism model. Left: photograph of a real-scale example (Amendola et al., 2014). Center and right: 3D view (center) and top view (right) of the geometric model.

Let H_{h_0} now denote the referential value of H_h (for $\mathbf{v} = \mathbf{v}_0 = [\ell_0, \varphi_0, h_0]^T$). The plots presented in Fig. 13 show the variation of H_{h_0} with the aspect ratio η_0 and the prestrain p_0, assuming $h_0 = 0.1$ m and the material constants of Table 1 (see Supplementary Data for the analytic expressions of H_h and H_{h_0} in the 'el' and the 'rigel' models). We let η_0 range in the interval $[0.01, 6.5]$ and p_0 vary between 0.05 and 0.4. It is worth noting that the thick prism model analyzed in Sect. 3.1 has aspect ratio η_0 varying between 0.91 (for $p_0 = 0$) and 0.94 ($p_0 = 0.4$, cf. Tab. 2), while the slender prism model analyzed in Sect. 3.2 has η_0 varying between 3.47 ($p_0 = 0$) and 4.48 ($p_0 = 0.4$, cf. Tab. 3). In correspondence with the examined values of η_0 and p_0, we observe that the response of the 'el' model in the reference configuration switches from stiffening ($H_{h_0} < 0$) to softening ($H_{h_0} > 0$) when one increases p_0 at constant η_0, or decreases η_0 at constant p_0. The referential response of the 'rigel' model is, instead, almost always stiffening, and undergoes softening only in the case of extremely thick geometries ($\eta_0 < 0.54$, cf. Fig. 13).

4. Experimental validation

The present section deals with an experimental validation of the models presented in Sections 2 and 3, against the results of quasi-static compression tests on physical samples (Amendola et al., 2014) (cf. also Section 3). We first examine the experimental responses of the thick prism specimens described in Table 4, where $N_1^{(0)}$ denotes the axial force carried by the cross-strings in correspondence with the reference configuration. Fig. 14 compares the theoretical ('th-el') and experimental ('exp-el') $F - \delta$ responses of such specimens, highlighting an overall good agreement between theory and experiments. We note a more compliant character of the experimental responses, as compared to those

α=β	p_0	s_N (m)	s_0 (m)	ℓ_N (m)	ℓ_0 (m)	b_N (m)	b_0 (m)	h_0 (m)	K_{h_0} (MN/m)
1	0	0.1620	0.1620	0.080	0.0800	0.1834	0.1834	0.1602	0.0000
1	0.005	0.1620	0.1628	0.080	0.0801	0.1842	0.1842	0.1610	0.0185
1	0.02	0.1620	0.1652	0.080	0.0804	0.1865	0.1865	0.1635	0.0676
1	0.05	0.1620	0.1701	0.080	0.0811	0.1911	0.1911	0.1684	0.1444
1	0.1	0.1620	0.1782	0.080	0.0821	0.1989	0.1989	0.1765	0.2364
1	0.2	0.1620	0.1944	0.080	0.0840	0.2143	0.2143	0.1928	0.3609
1	0.3	0.1620	0.2106	0.080	0.0856	0.2299	0.2299	0.2090	0.4549
1	0.4	0.1620	0.2268	0.080	0.0871	0.2454	0.2454	0.2253	0.5377
$\to \infty$	0	0.1620	0.1620	0.080	0.080	0.1834	0.1834	0.1602	0.0000
$\to \infty$	0.005	0.1620	0.1628	0.080	0.080	0.1841	0.1841	0.1610	0.0192
$\to \infty$	0.02	0.1620	0.1652	0.080	0.080	0.1863	0.1863	0.1635	0.0777
$\to \infty$	0.05	0.1620	0.1701	0.080	0.080	0.1906	0.1906	0.1684	0.1964
$\to \infty$	0.1	0.1620	0.1782	0.080	0.080	0.1979	0.1979	0.1766	0.4018
$\to \infty$	0.2	0.1620	0.1944	0.080	0.080	0.2126	0.2126	0.1929	0.8401
$\to \infty$	0.3	0.1620	0.2106	0.080	0.080	0.2275	0.2275	0.2092	1.3158
$\to \infty$	0.4	0.1620	0.2268	0.080	0.080	0.2425	0.2425	0.2255	1.8295

Table 3: Geometric variables and initial axial stiffness K_{h_0} of the slender prism model for different values of the cross-string prestrain p_0; the fully elastic model ($\alpha = \beta = 1$); and the rigid–elastic model ($\alpha = \beta \to +\infty$).

predicted by the fully-elastic model presented in Section 2, and oscillations of the experimental measurements. Such theory vs. experiment mismatches are explained by signal noise; progressive damage to the nodes during loading; string damage due to the rubbing of Spectra® fibers against the rivets placed at the nodes; and geometric imperfections (refer to Amendola et al. (2014) for detailed descriptions of such phenomena). In particular, geometric imperfections arising in the assembly phase prevent the three bars of the current prisms from simultaneously coming into contact with each other when the angle of twist approaches π. The marker $\oslash$ in Fig. 14 indicates the first configuration at which two bars touch each other, while the marker $\otimes$ indicates the first configuration with all three bars interfering. It is worth noting that the full locking configuration ('$\otimes$') occurs at an angle of twist φ appreciably lower than π, due to geometric imperfections and the nonzero thickness of the bars. Both the theoretical and experimental results shown in Fig. 14 indicate a clear softening character of the compressive response of the examined thick prisms.

type	p_0	s_N (m)	s_0 (m)	$N_1^{(0)}$(N)	ℓ_N (m)	ℓ_0 (m)	b_0 (m)
el	0.01	0.080	0.081	30.9	0.132	0.134	0.165
el	0.03	0.080	0.083	78.2	0.132	0.136	0.168
el	0.07	0.080	0.085	170.0	0.132	0.140	0.174

Table 4: Geometric and mechanical properties of thick prism samples.

We now pass to examining the experimental response of the slender prism specimens described in Table 5, which include two samples with deformable bases ('el' samples), and two samples aimed at reproducing the rigid–elastic model presented in Section 2.2 ('rigel' samples). The latter were assembled by replacing the base-strings of the 'el' systems

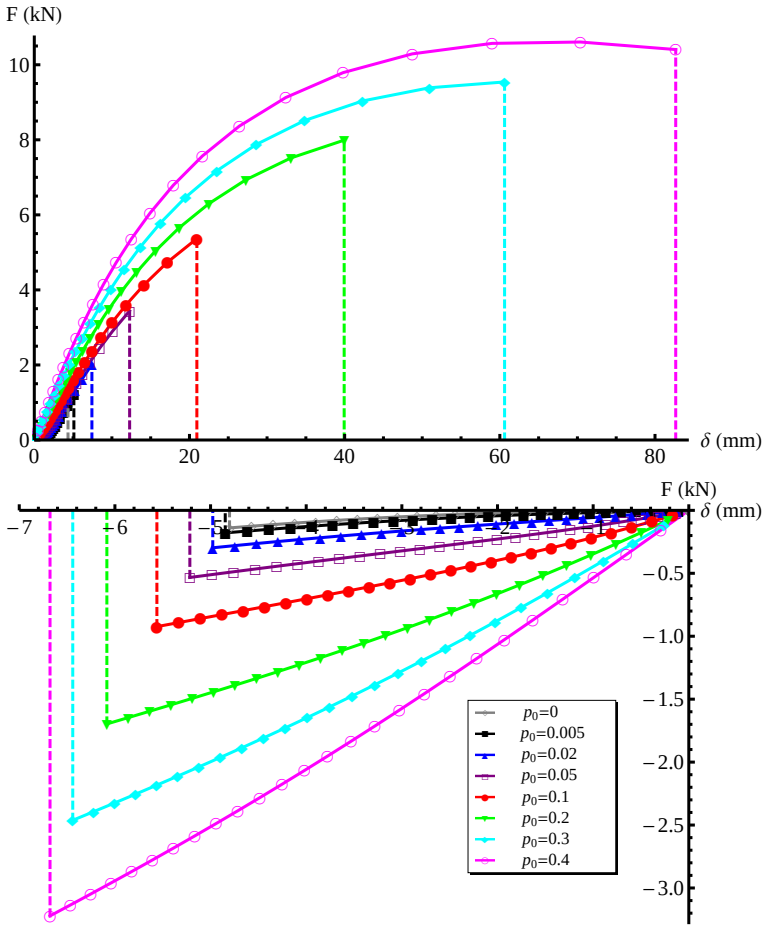

Figure 10: F–δ curves of the slender prism model, when loaded in compression (top), and tension (bottom), for $\alpha = \beta = 1$ and different values of p_0.

with 12 mm thick aluminum plates (cf. Fig. 15, and Amendola et al. (2014)). Fig. 16 illustrates a comparison between the theoretical and experimental responses of the 'el' samples, which shows a rather good match between theory and experiment. In the present case, we observe reduced signal noise, as compared to the case of thick prisms, and all the bars getting simultaneously in touch at locking. The main mismatch between the theoretical and experimental responses shown in Fig. 16 consists of an anticipated occurrence of prism locking in the physical models, which has already been observed and discussed in the case of the thick specimens. It is interesting to note that both the theoretical and the experimental results shown in Fig. 16 indicate a slightly stiffening behavior of the 'el' samples with a 'slender' aspect ratio.

The final experimental results presented in Fig. 17 are aimed at validating the rigid–elastic model presented in Section 2.2 ('rigel' samples). One observes that the examined specimens with nearly infinitely rigid bases feature a markedly stiff response in the proximity of the locking configuration, in line with the previsions of the model presented in Oppenheim and Williams (2000) for the current specimens. We observe a more compliant character of the experimental $F - \delta$ curves of 'rigel' samples, as compared to the theo-

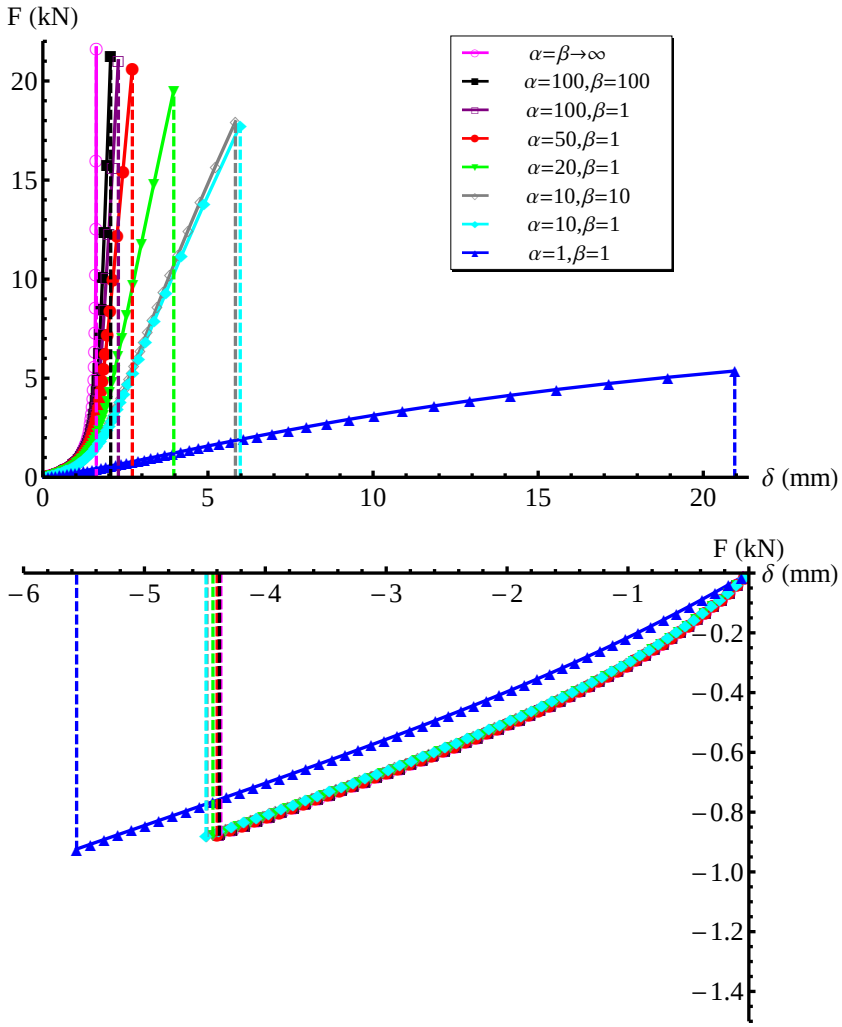

Figure 11: F–δ curves of the slender prism model, when loaded in compression (top), and tension (bottom), for $p_0 = 0.1$ and different values of α and β.

retical counterparts, which is explained by the not perfectly rigid behavior of the bases and the bars (physical samples), and the partial unthreading of the cross-strings from the lock washers placed at the the nodes (Amendola et al., 2014). The latter is induced by large tensile forces in the horizontal strings, when the system gets close to the locking configuration (cf. Supplementary Data).

type	p_0	s_N (m)	s_0 (m)	$N_1^{(0)}$(N)	ℓ_N (m)	ℓ_0 (m)	b_0 (m)
el	0.07	0.162	0.173	165.9	0.080	0.081	0.194
el	0.09	0.162	0.176	219.9	0.080	0.082	0.197
rigel	0.06	0.162	0.172	150.0	0.080	0.080	0.192
rigel	0.11	0.162	0.181	286.0	0.080	0.080	0.200

Table 5: Geometric and mechanical properties of slender prism samples.

5. Concluding remarks

We have presented a fully elastic model of axially loaded tensegrity prisms, which generalizes previous models available in the literature (Oppenheim and Williams, 2000;

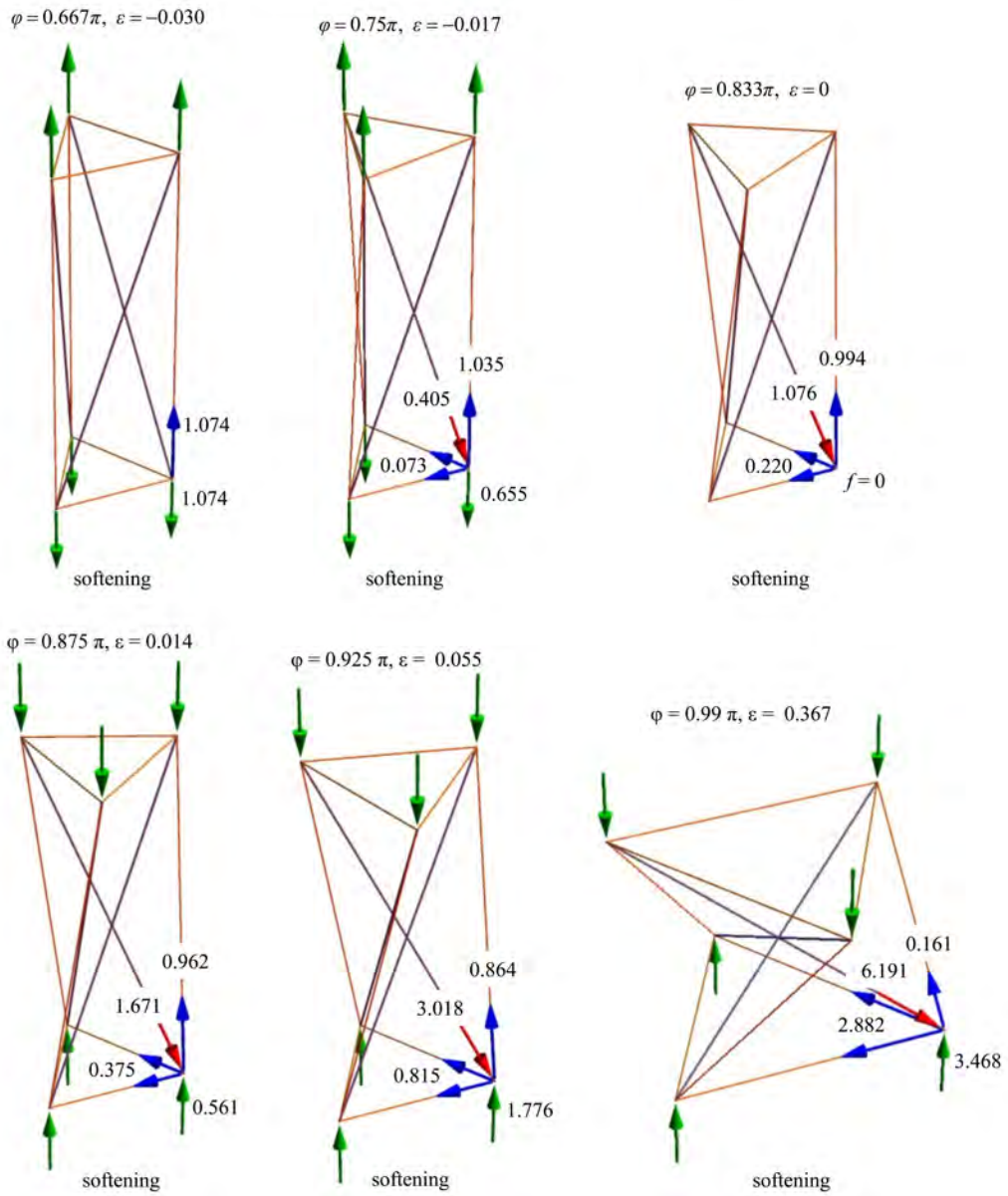

Figure 12: Member forces (kN) in different configurations of the slender prism, for $\alpha = \beta = 1$, and $p_0 = 0.4$.

Fraternali et al., 2012). The mechanical theory presented in Section 2.1 assumes that all the elements of a tensegrity prism respond as elastic springs, and relaxes the rigidity constraints introduced in Oppenheim and Williams (2000). On adopting the equilibrium approach to tensegrity systems described in Skelton and de Oliveira (2010), we have written the equilibrium equations in the current configuration, thus developng a geometrical nonlinear model allowing for large displacements (Section 2.1). In addition, we have presented an incremental formulation of the equilibrium problem of axially loaded tensegrity prisms, which is particularly useful when using Netwon's iterative schemes in numerical simulations (Section 2.1.3).

The numerical results presented in Section 3 highlight a rich variety of behaviors of tensegrity prisms under uniform axial loading and large displacements. The variegate mechanical response of such structures includes both extremely soft and markedly stiff de-

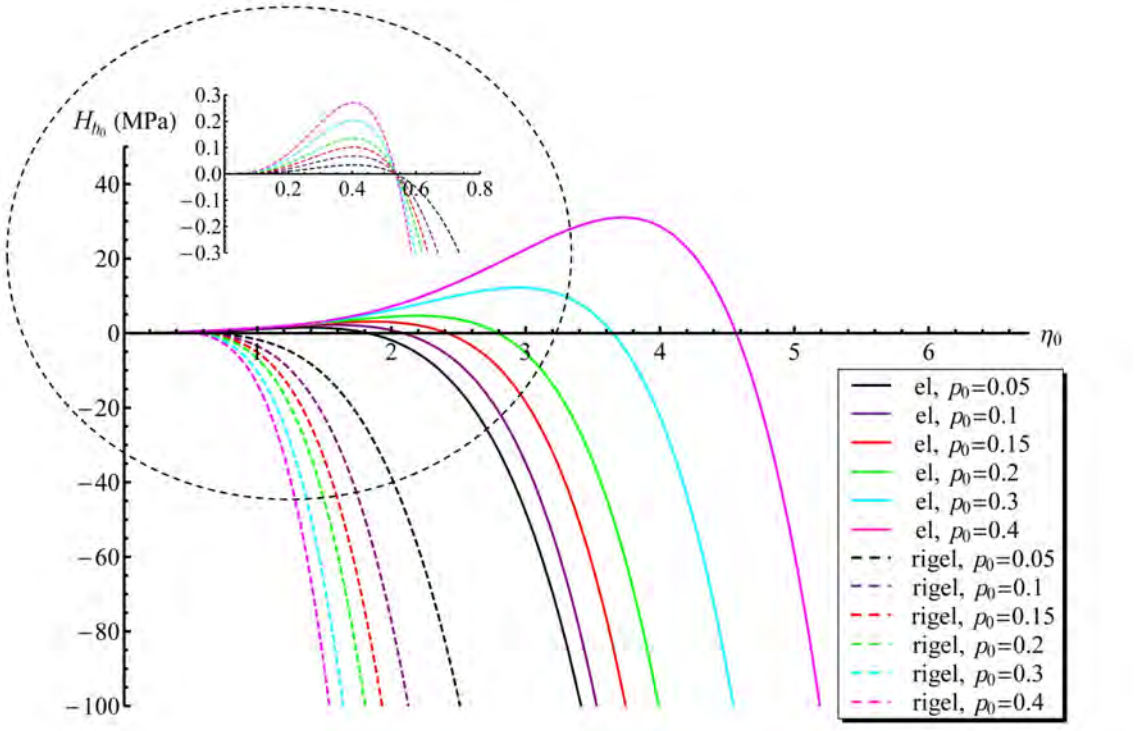

Figure 13: H_{h_0} versus η_0 plots for different values of the cross-string prestrain p_0. Inset: magnification of the $H_{h_0} - \eta_0$ plot of the 'rigel' model for $\eta_0 \leq 0.8$.

formation modes, depending on the geometry of the structure, the mechanical properties of the constituent elements, the magnitude of the cross-string prestrain p_0 (characterizing the whole state of self-stress), and the loading level (deformation-dependent behavior). We have found that 'thick' prisms exhibit softening response in compression under relatively low prestrains, and, on the contrary, stiffening response in tension over a large window of p_0 values (Figs. 4, 6, 8). The softening response in compression of such structures is often associated with a snap buckling event, which might lead the prism to axial collapse (prism height tending to zero). In contrast, we have noted that 'slender' prisms need large cable prestrains to show softening response in compression, and relatively low prestrains in order to feature softening response in tension (Fig. 10, 12, and Supplementary Data). By letting the base and bar rigidities tend to infinity, we have numerically observed that the compressive response of thick and slender prisms progressively switches to stiffening (Figs. 5, 7, 11), with the exception of extremely 'thick' geometries (cf. Sect. 3.3). In the rigid-elastic limit we have also noted that thick prisms typically exhibit stiffening response in tension (except for cases characterized by extremely high values of p_0, cf. Fig. 7), while slender prisms instead typically feature a slightly softening response in tension (cf. Fig. 11 and Supplementary Data). The softening response of prisms featuring a height h decreasing to zero is explained by the fact that the configuration with $h = 0$ necessarily shows zero axial force, since all members are horizontal. An experimental validation of the mechanical models presented in Section 2 has been conducted against the results of quasi-static compression tests on physical samples (Amendola et al., 2014), with good agreement between theory and experiments. The given experimental results

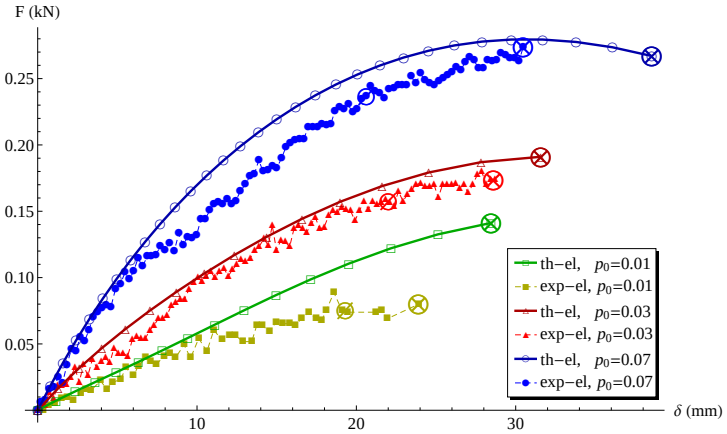

Figure 14: Comparison of the theoretical and experimental responses of thick prisms with deformable bases.

have confirmed the switching from softening to stiffening of the compressive response of the tested samples, in relation to the prism aspect ratio, the magnitude of the applied prestress, and the rigidity of the terminal bases.

The outcomes of the present study significantly enlarge the known spectrum of behavior of tensegrity prisms under axial loading, as compared to the literature to date (Oppenheim and Williams, 2000; Fraternali et al., 2012), and pave the way to the fabrication of innovative metamaterials featuring extremal (softening/stiffening) deformation modes. It has been shown in Fraternali et al. (2012) that 1D lattices of tensegrity prisms exhibiting elastic stiffening support extremely compact solitary waves. The 'atomic scale localization' of such waves (Friesecke and Matthies, 2002) may lead to create acoustic lenses capable of focusing pressure waves in very compact regions in space; to target tumors in hyperthermia applications; and to manufacture sensors/actuators for the non-destructive evaluation and monitoring of materials and structures (Spadoni and Daraio, 2010; Daraio and Fraternali, 2013). On the other hand, tensegrity lattices showing elastic softening can be used to design nonlinear metamaterials supporting special rarefaction waves, and innovative shock absorption devices that do not require energy dissipation (Herbold and Nesterenko, 2013).

This paper examines only one of many possible choices of tensegrity structures. Section 3.7 of Skelton and de Oliveira (2010) entitled 'Tensegrity Columns' shows a class 2 tower composed of either right-handed or left-handed prisms connected bar-to-bar. Alternative (class 1) columns are produced by stacking left-handed and right-handed prisms that are allowed to overlap, as in, the well-known tensegrity tower artworks by Kenneth Snelson (cf., e.g., Sects. 1.2 and 1.4.3 of Skelton and de Oliveira (2010)). In the near future, we intend to study the mechanical behavior of tensegrity columns, towers and plates by allowing the individual prisms to exhibit infinitesimal mechanisms (cf. Micheletti (2013)), and the overall structure to show geometrically nonlinear response. We also intend to investigate the dynamics of arrays of tensegrity columns, with the aim of generalizing available literature results on similar granular systems (Spadoni and Daraio, 2010). Intriguing mechanical behaviors are also offered by multistable tensegrity

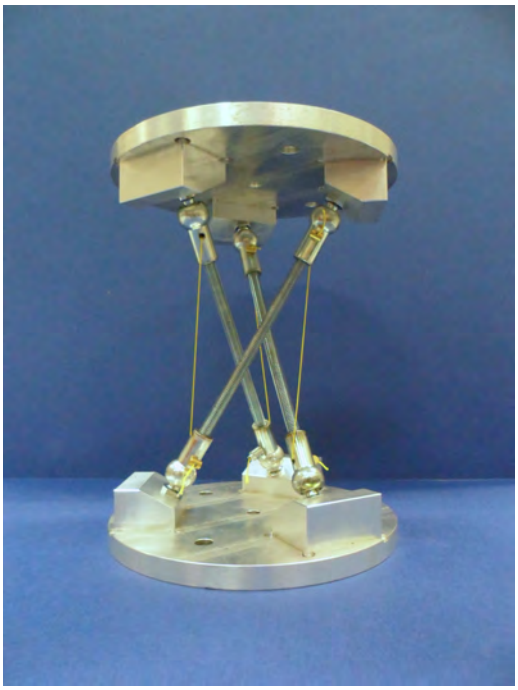

Figure 15: Photograph of a real-scale example of a slender prism endowed with thick aluminum bases (Amendola et al., 2014).

structures, and/or structures showing strings with zero or negative rest lengths (refer to Guest (2006, 2011); Schenk et al. (2007); Micheletti (2013); Favata et al. (2014), and the references therein, where the classification of tensegrity systems as 'prestress stable' or 'superstable' is introduced). The mechanical modeling of such structures is reserved for future studies, and comparisons with the results herein will be very insightful for the uncovered question of what is the best tensegrity metamaterial that matches a target (nonlinear) response law.

Particularly challenging is the topology optimization of 3D tensegrity lattices showing soft and hard units, with the aim of designing metamaterials featuring exceptional directional and band-gap properties (refer, e.g.., to Ruzzene and Scarpa (2005); Fraternali et al. (2010); Porter et al. (2009); Daraio et al. (2010); Ngo et al. (2012); Leonard et al. (2013); Manktelow et al. (2013); Casadei and Rimoli (2013); Skelton et al. (2014), and the references therein). The results of the present study highlight that the self-stresses of the basic units are peculiar design variables of tensegrity metamaterials, which can be finely tuned in order to switch the local response from softening to stiffening, according to given anisotropy patterns. Additional future extensions of the present study might involve the design of locally resonant metamaterials incorporating tensegrity concepts; the multiscale additive manufacturing of tensegrity structures through electron beam melting, laser lithography and/or projection micro-stereolithography (Grunsven et al., 2014; Bückmann et al., 2014; Zheng et al., 2012); and the numerical modeling of large-scale tensegrity lattices under general loading conditions, via the quasicontinuum method and local maximum-entropy schemes (Knap and Ortiz, 2001; Bompadre et al., 2012; Fraternali et al., 2012).

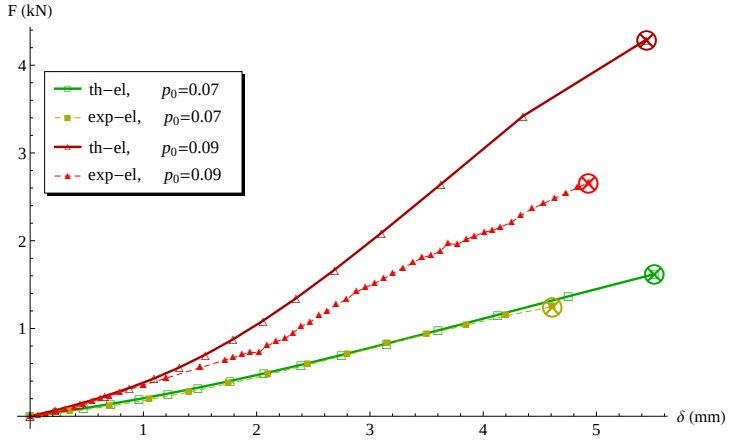

Figure 16: Comparison of the theoretical and experimental responses of slender prisms with deformable bases.

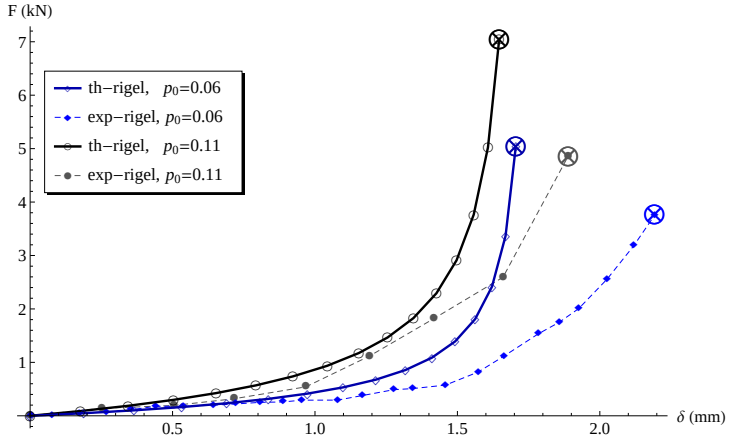

Figure 17: Comparison of the theoretical and experimental responses of slender prisms with rigid bases.

Acknowledgements

Support for this work was received from the Italian Ministry of Foreign Affairs, Grant No. 00173/2014, Italy-USA Scientific and Technological Cooperation 2014-2015 ('*Lavoro realizzato con il contributo del Ministero degli Affari Esteri, Direzione Generale per la Promozione del Sistema Paese*'). The authors would like to thank the anonymous referees for helpful comments, Robert Skelton and Mauricio de Oliveira (University of California, San Diego) for many useful discussions and suggestions, and Angelo Esposito (Department of Civil Engineering, University of Salerno) for his valuable assistance in the preparation of the numerical simulations.

Appendix. Supplementary Data

Supplementary Data associated with this article can be found in the online version.

References

Amendola, A., Fraternali, F., Carpentieri, G., de Oliveira, M., Skelton, R.E., 2014. Experimental investigation of the softening-stiffening response of tensegrity prisms under compressive loading. Compos. Struct. 117, 234-243.

Bertoldi, K., Boyce, M. C., 2008. Wave propagation and instabilities in monolithic and periodically structured elastomeric materials undergoing large deformations. Phys. Rev. B 78(18), 184107.

Bigoni, D., Guenneau, S., Movchan, A. B., Brun, M., 2013. Elastic metamaterials with inertial locally resonant structures: Application to lensing and localization. Phys. Rev. B 87(174303), 1–6.

Bompadre, A., Schmidt, B., Ortiz, M., 2012. Convergence analysis of meshfree approximation schemes. SIAM J. Numer. Anal. 50(3), 1344–1366.

Brunet, T., Leng, J., Mondain-Monval, O., 2013. Soft acoustic metamaterials. Science 342, 323–324.

Böckmann,T., Thiel, M., Kadic, M., Schittny, R., Wegener, M., 2014. An elastomechanical unfeelability cloak made of pentamode metamaterials. Nature Communications 5, 4130.

Casadei, F., Rimoli, J. J., 2013. Anisotropy-induced broadband stress wave steering in periodic lattices. Int. J. Solids Struct. 50(9), 1402–1414.

Daraio, C., Nesterenko, V. F., Herbold, E. B., Jin, S., 2006. Energy trapping and shock disintegration in a composite granular medium. Phys. Rev. Lett. 96, 058002.

Daraio, C., Ngo, D., Nesterenko, V.F., Fraternali, F., 2010. Highly nonlinear pulse splitting and recombination in a two-dimensional granular network. Phys. Rev. E 82, 036603.

Daraio, C., Fraternali, F., 2013. Method and Apparatus for Wave Generation and Detection Using Tensegrity Structures. US Patent No. 8,616,328.

Engheta, N., Ziolkowski, R. W., 2006. Metamaterials: Physics and engineering explorations. J. Wiley and Sons, Philadelphia.

Fang, N., Xi, D., Xu, J., Muralidhar, Ambati, M., Srituravanich, W., Werayut, S., Sun, C., Zhang, X., 2006. Ultrasonic metamaterials with negative modulus. Nat. Mater. 5, 452–456.

Favata, A., Micheletti, A., Podio–Guidugli, P., 2014. A nonlinear theory of prestressed elastic stick–and–spring structures. Int. J. Eng. Sci. 80, 4–20.

Fraternali, F., Lorenz, C. D., Marcelli, G., 2012. On the estimation of the curvatures and bending rigidity of membrane networks via a local maximum-entropy approach. J. Comput. Phys. 231(2), 528–540.

Fraternali, F., Porter, M., and Daraio, C., 2010. Optimal design of composite granular protectors. Mech. Adv. Mat. Struct. 17, 1–19.

Fraternali, F., Senatore, L. and Daraio, C., 2012. Solitary waves on tensegrity lattices. J.Mech. Phys. Solids 60, 1137–1144.

Friesecke, G. and Matthies, K., 2002. Atomic-scale localization of high-energy solitary waves on lattices. Physica D 171, 211–220.

Gonella, S., Ruzzene, M., 2008. Analysis of in-plane wave propagation in hexagonal and re-entrant Lattices. J. Sound Vib. 312(1-2), 125–139.

van Grunsven, W., Hernandez-Nava, E., Reilly, G.C., Goodall, R., 2014. Fabrication and mechanical characterisation of titanium lattices with graded porosity Metals, 4(3), 401–409.

Guest, S., 2006. The stiffness of prestressed frameworks: A unifying approach. Int. J. Solid Struct 43, 842–854.

Guest, S. D., 2011. The stiffness of tensegrity structures. IMA J. Appl. Math. 76(1), 57–66.

Herbold, E. B. and Nesterenko, V. F., 2013. Propagation of rarefaction pulses in discrete materials with strain-softening behavior. Phys. Rev. Lett. 110, 144101.

Kadic, M., Bckmann, T., Stenger, N., Thiel, M. and Wegener, M., 2012. On the practicability of pentamode mechanical metamaterials. Appl. Phys. Lett. 100(19).

Kashdan, L., Seepersad, C. C., Haberman, M., Wilson, P. S., 2012. Design, fabrication, and evaluation of negative stiffness elements using SLS. Rapid Prototyping J. 18(3), 194–200.

Kochmann, D. M., and Venturini, G. N., 2013. Homogenized mechanical properties of auxetic composite materials in finite-strain elasticity. Smart mater. Struct., 22(8), 084004.

Kochmann, D. M., 2014. Stable extreme damping in viscoelastic two-phase composites with non-positive- definite phases close to the loss of stability. Mech. Res. Commun., 58, 36–45.

Knap, J. and Ortiz, M., 2001 An analysis of the quasicontinuum method. J.Mech. Phys. Solids 49, 1899–1923.

Lakes, R. S., 1987. Foam Structures with a Negative Poisson's Ratio. Science 235, 1038–1040.

Lee, H., Zhang, J., Jiang, H., and Fang, N. X., 2012. Prescribed pattern transformation in swelling gel tubes by elastic instability. Phys. Rev. Lett., 108, 214304.

Leonard, A. and Fraternali, F. and Daraio, C., 2013. Directional Wave Propagation in a Highly Nonlinear Square Packing of Spheres. Exp. Mech. 53(3), 327–337.

Li, J., Chan, C. T., 2004. Double-negative acoustic metamaterial. Phys. Rev. E 70 (5 2), 055602-1–055602-4.

Liu, Q., 2006. Literature Review: Materials with Negative Poisson's Ratios and Potential Applications to Aerospace and Defence. DTIC Document. No. DSTO-GD-0472. Defence science and technology organization Victoria (Australia) Air Vehicles DIV.

Liu, Z., Zhang, X., Mao, Y., Zhu, Y. Y., Yang, Z., Chan, C. T., Sheng, P., 2000. Locally Resonant Sonic Materials. Science 289(5485), 1734–1736.

Lu, M.H., Feng, L., Chen,Y.F., 2009. Phononic Crystals and Acoustic Metamaterials. Mater. Today 12(12), 34–42.

Manktelow, K.L., Leamy, M.J., Ruzzene, M., 2013. Topology design and optimization of nonlinear periodic materials. J. Mech. Phys. Solids 61(12), 2433–2453.

Micheletti, A., 2013. Bistable Regimes in an Elastic Tensegrity System. P. Roy. Soc. 469(2154), 201300520.

Milton, G. W., 1992. Composite materials with Poisson's ratios close to -1. J. Mech. Phys. Solids 40(5), 1105–1137.

Milton, G. W., 2002. The theory of composites. Cambridge University Press, Salt Lake City.

Milton, G. W., 2013. Adaptable nonlinear bimode metamaterials using rigid bars, pivots, and actuators. J. Mech. Phys. Solids 61, 1561–1568.

Milton, G. W. and Cherkaev, A. V., 1995. Which Elasticity Tensors are Realizable? J. Eng. Mater. Technol. 117(4), 483–493.

Nesterenko, V.F., 2001. Dynamics of Heterogeneous Materials. Springer, New York.

Ngo, D., Fraternali, F., Daraio, C., 2012. Highly nonlinear solitary wave propagation in Y-shaped granular crystals with variable branch angles. Phys. Rev. E 85, 036602.

Nicolaou, Z. G., Motter, A. E., 2012. Mechanical metamaterials with negative compressibility transitions. Nat. Mater. 11, 608–613.

Oppenheim, I. and Williams, W., 2000. Geometric effects in an elastic tensegrity structure. J. Elast. 59, 51–65.

Porter, M.A., Daraio, C., Szelengowicz, I., Herbold, E.B., Kevrekidis, P.G., 2009. Highly nonlinear solitary waves in heterogeneous periodic granular media. Physica D 238(6), 666–676.

Riks, E., 1984. Some computational aspects of the stability analysis ofnonlinear structures. Int. J. Solids Struct. 47, 219–259.

Ruzzene, M., Scarpa, F., 2005. Directional and band gap behavior of periodic auxetic lattices. Phys. Status Solidi B 242(3), 665–680.

Schenk, M., Guest, S. D., Herder, J. L., 2007. Zero stiffness tensegrity structures. Int. J. Solids Struct. 44, 6569–6583.

Skelton, R. E. and de Oliveira, M. C., 2010. Tensegrity Systems. Springer, New York.

Skelton, R. E., Fraternali, F., Carpentieri, G., Micheletti, A., 2014. Minimum mass design of tensegrity bridges with parametric architecture and multiscale complexity. Mech. Res. Commun., 58, 124–132.

Spadoni, A. and Daraio, C., 2010. Generation and control of sound bullets with a nonlinear acoustic lens. Proc. Natl. Acad. Sci. U.S.A. 107(16), 7230–7234.

Spadoni, A., Ruzzene, M., 2012. Elasto-static micropolar behavior of a chiral auxetic lattice. J. Mech. Phys. Solids 60(1), 156–171.

Wang, P., Shim, J., Bertoldi, K., 2013. Effects of geometric and material nonlinearities on tunable band gaps and low-frequency directionality of phononic crystals. Phys. Rev. B 88(014304), 1-15.

Wriggers, P., Simo, J.C., 1990. A general procedure for the direct computation of turning and bifurcation points. Int. J. Numer. Meth. Eng., 30(1), 155–176.

Zhang, S., Yin, L., Fang, N., 2009. Focusing Ultrasound with an Acoustic Metamaterial Network. Phys. Rev. Lett. 102(194301), 1–4.

Zhang, S., 2010. Acoustic metamaterial design and application. Ph.D. Thesis, University of Illinois at Urbana-Champaign, `http://web.mit.edu/nanophotonics/projects/Dissertation_Shu.pdf`.

Zheng, X., Deotte, J., Alonso, M. P., Farquar, G. R., Weisgraber, T. H., Gemberling, S., Lee, H., Fang, N., Spadaccini, C. M., 2012. Design and optimization of a light-emitting diode projection micro-stereolithography three-dimensional manufacturing system. Rev. Sci. Instrum., 83, 125001.

Supporting online material for
On the mechanical modeling of the extreme softening/stiffening response of axially loaded tensegrity prisms

F. Fraternali, G. Carpentieri, A. Amendola

Department of Civil Engineering, University of Salerno,84084 Fisciano(SA), Italy

Abstract

We present some additions to the article *'On the mechanical modeling of the extreme softening/stiffening response of axially loaded tensegrity prisms'*, to be published alongside its online version. This addendum includes analytic results on the axial stiffness of a minimal regular tensegrity prism K_h; the Mathematica® code 'Kh_formulas' providing analytic formulas of K_h and its derivative H_h; two movies showing animations of the force-displacement response of a thick elastic prism (movie1.avi), and a rigid-elastic slender prism (movie2.avi); and several plots illustrating the mechanical response of a slender prism model.

Appendix A. Axial stiffness of a minimal regular tensegrity prism

Let us examine the matrix $\mathbf{V}$ introduced in Sect. 2.1 of the main paper. It is not difficult to verify that the entries of such a matrix have the following analytic expressions (see the enclosed Mathematica® code 'Kh_formulas.nb')

$$
\begin{aligned}
V_{11} \;=\; & \frac{1}{6}\Bigg\{4k_3\sin^2\left(\frac{\varphi}{2}\right)\left(\sqrt{3}-\frac{9h^2b_N}{\left(3h^2-2\ell^2\cos(\varphi)+2\ell^2\right)^{3/2}}\right)+\Big(k_1 \\
& \times\Bigg(\sqrt{3h^2-\sqrt{3}\ell^2\sin(\varphi)+\ell^2\cos(\varphi)+2\ell^2}\Big(-9h^2\sin(\varphi)+\sqrt{3}\left(3h^2+4\ell^2\right) \\
& \times\cos(\varphi)+6\sqrt{3}h^2-12\ell^2\sin(\varphi)-3\ell^2\sin(2\varphi)-\sqrt{3}\ell^2\cos(2\varphi)+6\sqrt{3}\ell^2\Big) \\
& -9h^2s_N(-\sqrt{3}\sin(\varphi)+\cos(\varphi)+2)\Bigg)\Big)/\Big(\Big(3h^2-\sqrt{3}\ell^2\sin(\varphi)+\ell^2\cos(\varphi) \\
& +2\ell^2\Big)^{3/2}\Big)+6\sqrt{3}k_2\Bigg\} \qquad (1)
\end{aligned}
$$

Email addresses: f.fraternali@unisa.it (F. Fraternali), gcarpentieri@unisa.it (G. Carpentieri), adamendola@gmail.com (A. Amendola)

$$
\begin{aligned}
V_{12} &= \frac{1}{6}\ell\left(\frac{2k_3\sin(\varphi)\left(\sqrt{3}\left(3h^2-2\ell^2\cos(\varphi)+2\ell^2\right)^{3/2}-3b_N\left(3h^2-\ell^2\cos(\varphi)+\ell^2\right)\right)}{\left(3h^2-2\ell^2\cos(\varphi)+2\ell^2\right)^{3/2}}\right. \\
&\quad -\left(k_1\left(2\sqrt{3h^2-\sqrt{3}\ell^2\sin(\varphi)+\ell^2\cos(\varphi)+2\ell^2}\left(\left(9h^2+6\ell^2\right)\cos(\varphi)+\sqrt{3}\right.\right.\right. \\
&\quad \times\sin(\varphi)\left(3h^2-2\ell^2\cos(\varphi)+2\ell^2\right)+3\ell^2\cos(2\varphi)\big)-3s_N\left(2\sqrt{3}\left(3h^2+\ell^2\right)\right. \\
&\quad \left.\left.\left.\times\cos(\varphi)+2\sin(\varphi)\left(3h^2-\ell^2\cos(\varphi)+\ell^2\right)+\sqrt{3}\ell^2\cos(2\varphi)\right)\right)\right)/\Big(2\Big(3h^2 \\
&\quad \left.-\sqrt{3}\ell^2\sin(\varphi)+\ell^2\cos(\varphi)+2\ell^2\Big)^{3/2}\right)\Big) \qquad (2)
\end{aligned}
$$

$$
\begin{aligned}
V_{13} &= \frac{3}{2}h\ell\left(\frac{4k_3b_N\sin^2\left(\frac{\varphi}{2}\right)}{\left(3h^2-\ell^2\left(2\cos(\varphi)+2\right)\right)^{3/2}}\right. \\
&\quad \left.+\frac{k_1s_N\left(-\sqrt{3}\sin(\varphi)+\cos(\varphi)+2\right)}{\left(3h^2-\ell^2\left(\sqrt{3}\sin(\varphi)+\cos(\varphi)+2\right)\right)^{3/2}}\right) \qquad (3)
\end{aligned}
$$

$$
\begin{aligned}
V_{21} &= \frac{1}{6}\left(2k_3\sin(\varphi)\left(\frac{9h^2b_N}{\left(3h^2-2\ell^2\cos(\varphi)+2\ell^2\right)^{3/2}}-\sqrt{3}\right)+(k_1\right. \\
&\quad \times\left(\sqrt{3h^2-\sqrt{3}\ell^2\sin(\varphi)+\ell^2\cos(\varphi)+2\ell^2}\left(\left(9h^2+6\ell^2\right)\cos(\varphi)+\sqrt{3}\sin(\varphi)\right.\right. \\
&\quad \left.\left.\times\left(3h^2-2\ell^2\cos(\varphi)+2\ell^2\right)+3\ell^2\cos(2\varphi)\right)-9h^2s_N\left(\sin(\varphi)+\sqrt{3}\cos(\varphi)\right)\right)\Big) \\
&\quad /\left(\left(3h^2-\sqrt{3}\ell^2\sin(\varphi)+\ell^2\cos(\varphi)+2\ell^2\right)^{3/2}\right)\Big) \qquad (4)
\end{aligned}
$$

$$
\begin{aligned}
V_{22} &= \frac{1}{6}\ell\left(2k_3\left(-\frac{3b_N\left(\ell^2(\cos(2\varphi)+3)-2\left(3h^2+2\ell^2\right)\cos(\varphi)\right)}{2\left(3h^2-2\ell^2\cos(\varphi)+2\ell^2\right)^{3/2}}-\sqrt{3}\cos(\varphi)\right)\right. \\
&\quad +\Big(k_1\Big(3s_N\Big(6\sqrt{3}h^2\sin(\varphi)-2\left(3h^2+2\ell^2\right)\cos(\varphi)+4\sqrt{3}\ell^2\sin(\varphi)+\sqrt{3}\ell^2 \\
&\quad \times\sin(2\varphi)+\ell^2\cos(2\varphi)-6\ell^2\Big)+2\sqrt{3h^2-\sqrt{3}\ell^2\sin(\varphi)+\ell^2\cos(\varphi)+2\ell^2} \\
&\quad \times\Big(-9h^2\sin(\varphi)+\sqrt{3}\left(3h^2+2\ell^2\right)\cos(\varphi)-6\ell^2\sin(\varphi)-3\ell^2\sin(2\varphi)-\sqrt{3}\ell^2 \\
&\quad \left.\times\cos(2\varphi)+2\sqrt{3}\ell^2\Big)\Big)\Big)/\left(2\left(3h^2-\sqrt{3}\ell^2\sin(\varphi)+\ell^2\cos(\varphi)+2\ell^2\right)^{3/2}\right)\right) \qquad (5)
\end{aligned}
$$

$$
\begin{aligned}
V_{23} &= \frac{3}{2}h\ell\left(\frac{k_1s_N\left(\sin(\varphi)+\sqrt{3}\cos(\varphi)\right)}{\left(3h^2-\sqrt{3}\ell^2\sin(\varphi)+\ell^2\cos(\varphi)+2\ell^2\right)^{3/2}}\right. \\
&\quad \left.-\frac{2k_3b_N\sin(\varphi)}{\left(3h^2-2\ell^2\cos(\varphi)+2\ell^2\right)^{3/2}}\right) \qquad (6)
\end{aligned}
$$

$$V_{31} = \frac{1}{2}\sqrt{3}h\left(-\frac{8k_3\ell b_N \sin^2\left(\frac{\varphi}{2}\right)}{\left(3h^2-2\ell^2\cos(\varphi)+2\ell^2\right)^{3/2}} - \frac{2k_1\ell s_N\left(-\sqrt{3}\sin(\varphi)+\cos(\varphi)+2\right)}{\left(3h^2-\sqrt{3}\ell^2\sin(\varphi)+\ell^2\cos(\varphi)+2\ell^2\right)^{3/2}}\right) \quad (7)$$

$$V_{32} = \frac{1}{2}\sqrt{3}h\ell^2\left(\frac{k_1 s_N\left(\sin(\varphi)+\sqrt{3}\cos(\varphi)\right)}{\left(3h^2-\sqrt{3}\ell^2\sin(\varphi)+\ell^2\cos(\varphi)+2\ell^2\right)^{3/2}} - \frac{2k_3 b_N\sin(\varphi)}{\left(3h^2-2\ell^2\cos(\varphi)+2\ell^2\right)^{3/2}}\right) \quad (8)$$

$$V_{33} = k_3\left(\frac{4\sqrt{3}\ell^2 b_N\sin^2\left(\frac{\varphi}{2}\right)}{\left(3h^2-2\ell^2\cos(\varphi)+2\ell^2\right)^{3/2}}-1\right) + k_1\left(-\frac{\sqrt{3}\ell^2 s_N\left(\sqrt{3}\sin(\varphi)-\cos(\varphi)-2\right)}{\left(3h^2-\sqrt{3}\ell^2\sin(\varphi)+\ell^2\cos(\varphi)+2\ell^2\right)^{3/2}}-1\right) \quad (9)$$

By inserting the above results into Eqn. (32) of the main paper, we easily obtain the axial stiffness K_t^{el} of the fully-elastic model. The reference value of such a quantity (for $\ell=\ell_0, \varphi=\varphi_0, h=h_0$) can be written as follows

$$\begin{aligned} K_{h_0}^{el} = {} & \frac{p_0}{1+p_0}\Bigg\{36k_1\eta_0^2\Bigg((3+2\sqrt{3}+\sqrt{3}\eta_0^2)k_1k_2+(-2+\sqrt{3}-\eta_0^2)k_1k_1\frac{p_0}{1+p_0} \\ & -6k_2k_1\frac{p_0}{1+p_0}+k_3(2\sqrt{3}k_1+(-3+2\sqrt{3}+\sqrt{3}\eta_0^2)k_2-(2+\sqrt{3}+\eta_0^2) \\ & \times k_1\frac{p_0}{1+p_0})\Bigg)\Bigg\} / \Bigg\{6k_1\frac{p_0}{1+p_0}\left(\sqrt{3}(1+8\eta_0^2+2\eta_0^4)k_2-2\eta_0^4k_1\frac{p_0}{1+p_0}\right) \\ & +k_1\Big(3(2+\sqrt{3}+\eta_0^2)k_2+(-3+2\sqrt{3}+(-24+13\sqrt{3})\eta_0^2)k_1\frac{p_0}{1+p_0}\Big) \\ & +k_3\Big(6k_1+3(2-\sqrt{3}+\eta_0^2)k_2+(3+2\sqrt{3}+(24+13\sqrt{3})\eta_0^2)k_1\frac{p_0}{1+p_0}\Big)\Bigg\} \end{aligned} \quad (10)$$

where:

$$\eta_0 = \frac{h_0}{a_0} \quad (11)$$

For what concerns the rigid-elastic model (cf. Sect. 2.2 of the main paper), we easily obtain

$$
\begin{aligned}
{K_h}^{rigel}(h) \;=\; & \frac{1}{2a^4(2\sqrt{3}a^2\cos(\varphi+\frac{\pi}{6})+b^2)^{3/2}}\Bigg\{3k_1\csc^3(\varphi)\Big[\sqrt{3}\sin(\varphi+\frac{\pi}{6})\,\big(a^4 \\
& \times(\cos(2\varphi)+3)+2a^2(b^2-2a^2)\cos(\varphi)\big)\,(2\sqrt{3}a^2\cos(\varphi+\frac{\pi}{6})+b^2) \\
& \times\Big(\sqrt{2\sqrt{3}a^2\cos(\varphi+\frac{\pi}{6})+b^2}-s_N\Big)-2a^2\sin(\varphi)(2a^2\cos(\varphi)-2a^2 \\
& +b^2)\Bigg(\cos(\varphi+\frac{\pi}{6})(6a^2\cos(\varphi+\frac{\pi}{6})+\sqrt{3}b^2)\sqrt{2\sqrt{3}a^2\cos(\varphi+\frac{\pi}{6})+b^2} \\
& -s_N\left(3a^2\sin^2(\varphi+\frac{\pi}{6})+6a^2\cos^2(\varphi+\frac{\pi}{6})+\sqrt{3}b^2\cos(\varphi+\frac{\pi}{6})\right)\Bigg)\Big]\Bigg\} \qquad (12)
\end{aligned}
$$

$$
K_{h_0}^{rigel} \;=\; -F'(h=h_0) \;=\; 12\,\sqrt{3}\,k_1\frac{p_0}{1+p_0}\,\eta_0^2 \qquad (13)
$$

The Mathematica® code 'Kh_formulas' provides the general expressions of K_h and the derivative H_h of K_h with respect to h, for both the elastic and the rigid-elastic models.

Appendix B. Movies

The movies 'movie1.avi' and 'movie2.avi' show animations of the force-displacement response of a thick elastic prism (movie1.avi: case with $\alpha=\beta=1$ and $p_0=0.1$ in Tab. 2 of the main paper), and a rigid-elastic slender prism (movie2.avi: case with $\alpha=\beta\to\infty$ and $p_0=0.1$ in Tab. 3 of the main paper).

Appendix C. Additional results on the mechanical response of the 'slender' prism model

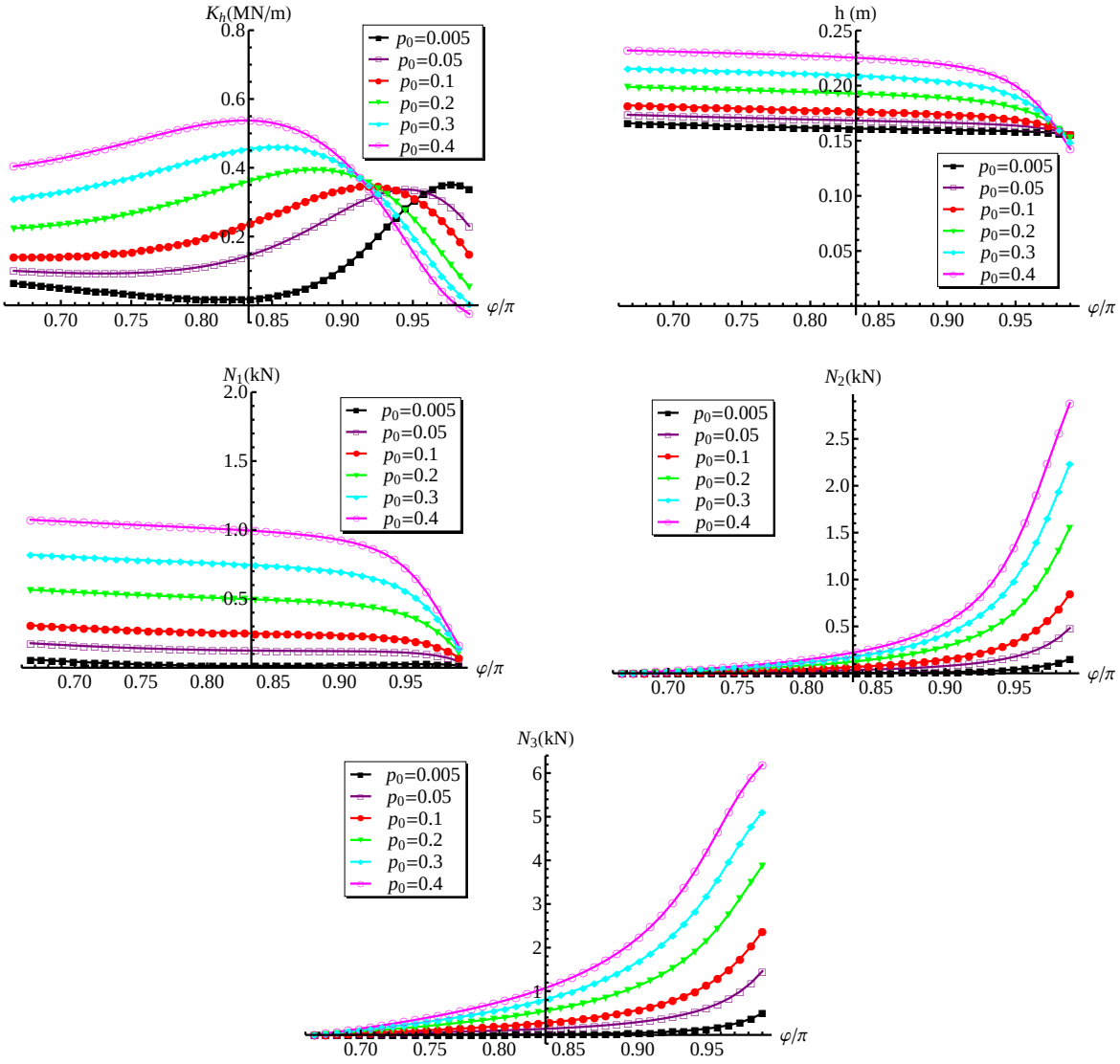

Figure 1: K_h vs. φ, h vs. φ and N_1, N_2, N_3 vs. φ curves of the slender prism model for $\alpha = \beta = 1$, and different values of p_0.

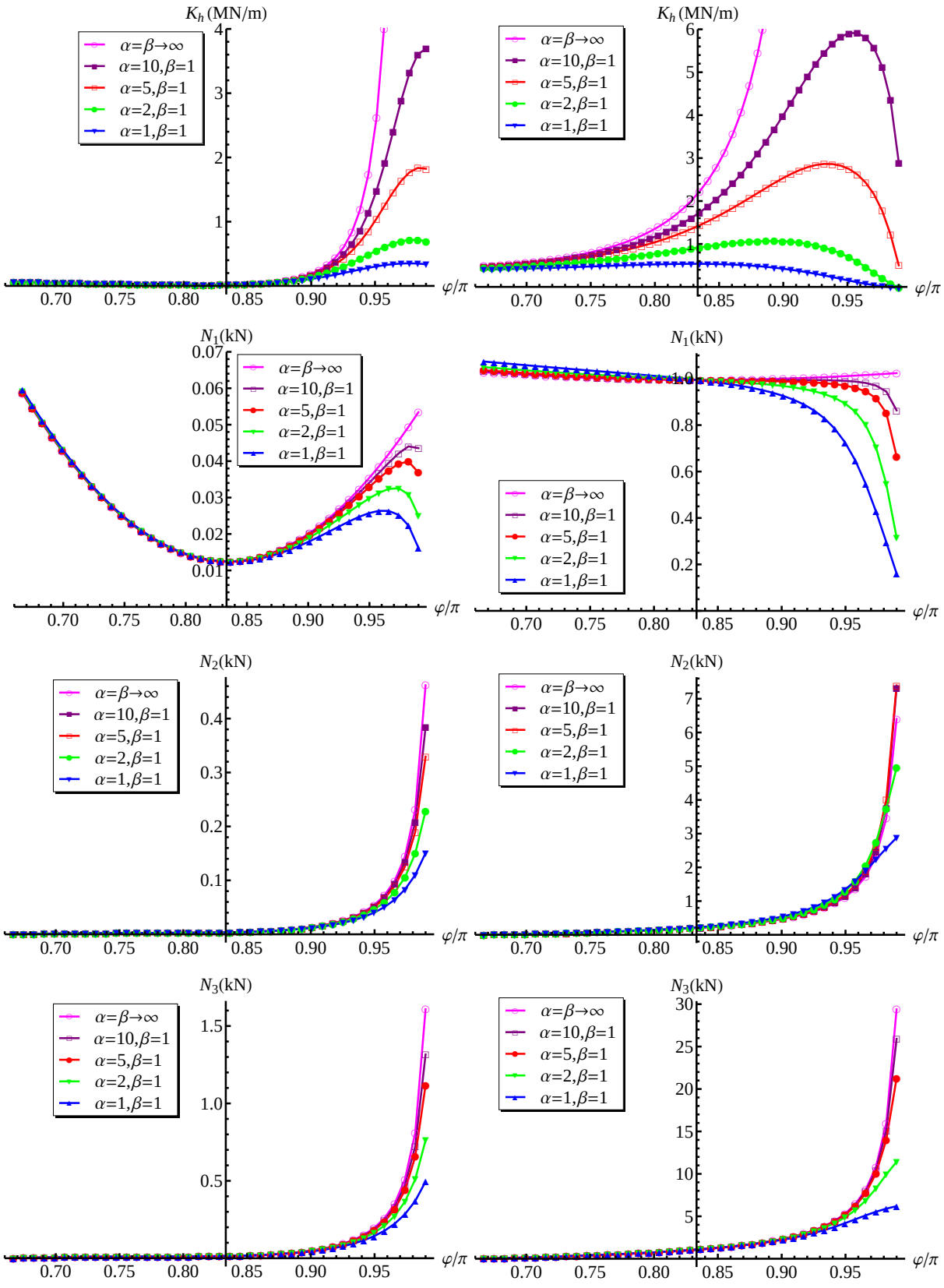

Figure 2: K_h vs. φ and N_1, N_2, N_3 vs. φ curves of the slender prism model for $p_0 = 0.005$ (left), $p_0 = 0.4$ (right) and different values of α and β.

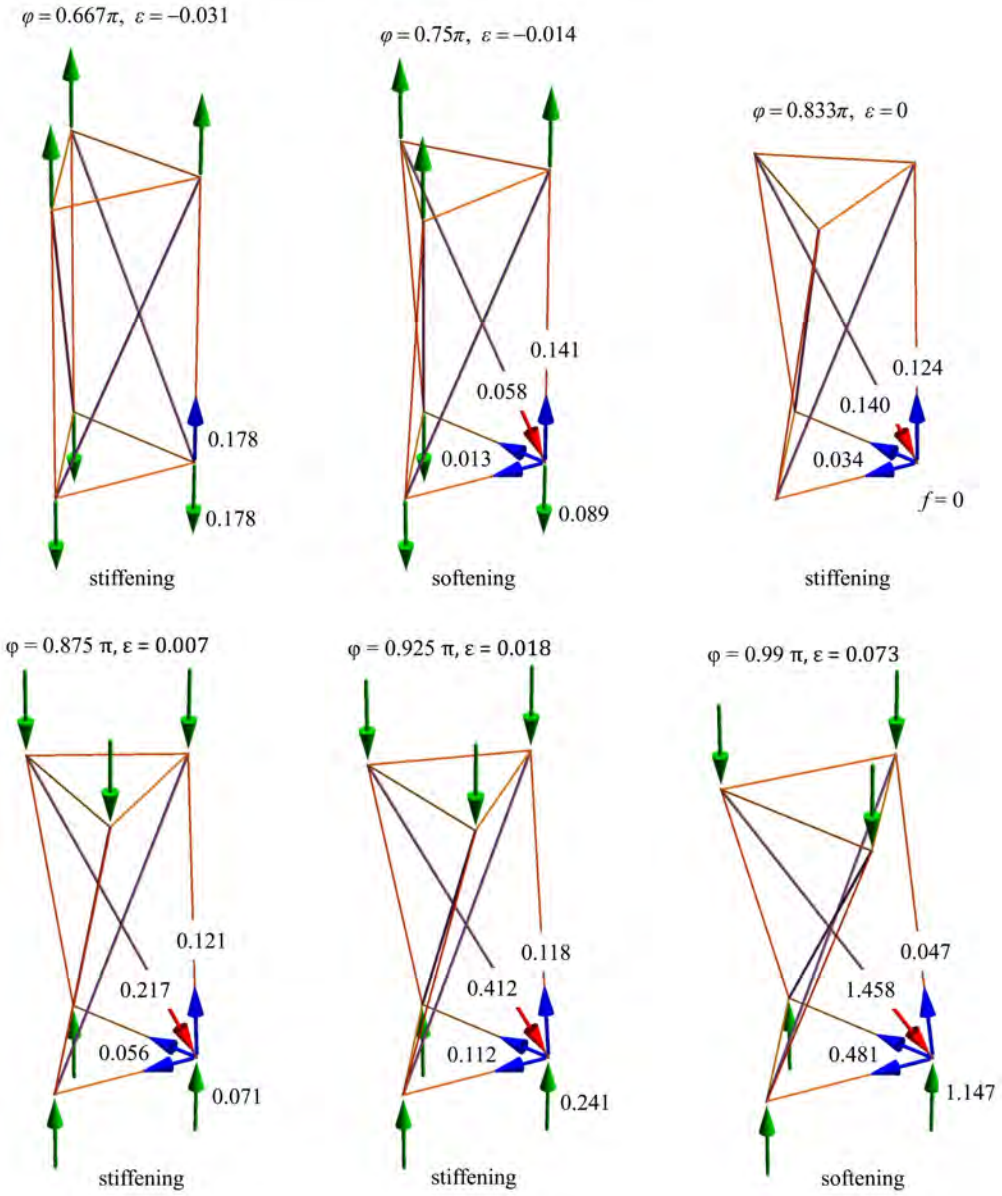

Figure 3: Member forces (kN) in different configurations of the slender prism model, for $\alpha = \beta = 1$, and $p_0 = 0.05$.